Recovering doping profiles in semiconductor devices with the Boltzmann-Poisson model

Yingda Cheng* Irene M. Gamba† Kui Ren‡

August 6, 2010

Abstract

We investigate numerically an inverse problem related to the Boltzmann-Poisson system of equations for transport of electrons in semiconductor devices. The objective of the (ill-posed) inverse problem is to recover the doping profile of a device, presented as source function in the mathematical model, from its current-voltage characteristics. To reduce the degree of ill-posedness of the inverse problem, we proposed to parameterize the unknown doping profile function to limit the number of unknowns in the inverse problem. We showed by numerical examples that the reconstruction of a few low moments of the doping profile is possible when relatively accurate time-dependent or time-independent measurements are available, even though the later reconstruction is less accurate than the former. We also compare reconstructions from the Boltzmann-Poisson (BP) model to those from the classical drift-diffusion-Poisson (DDP) model, assuming that measurements are generated with the BP model. We show that the two type of reconstructions can be significantly different in regimes where drift-diffusion-Poisson equation fails to model the physics accurately. However, when noise presented in measured data is high, no difference in the reconstructions can be observed.

Key words. Boltzmann-Poisson system, semiconductor devices, doping profile, inverse problems, parameter identification, inverse doping, drift-diffusion.

1 Introduction

Parameter extraction for semiconductor devices play a key role in modern semiconductor device design and performance optimization. The aim of parameter extraction is to recover material parameters of devices from measurement of device characteristics, such as the voltage-to-current (I-V) data and the voltage-to-capacitance (C-V) data. The parameters

*Department of Mathematics and ICES, University of Texas, Austin, TX 78712; Email: ycheng@math.utexas.edu.

†Department of Mathematics and ICES, University of Texas, Austin, TX 78712; Email: gamba@math.utexas.edu.

‡Department of Mathematics, University of Texas, Austin, TX 78712; Email: ren@math.utexas.edu.

that are of interests are mainly the doping profile [19, 24, 34, 47] and the carrier mobilities [10, 51, 56], but there are also significant interests in other material parameters such as thermal and electrical conductivities [30, 31].

In this paper, we are mainly interested in the recovery of the doping profiles of semiconductor devices. The most widely used technique in the semiconductor community is the so-called C-V technique, proposed initially by Kennedy, Murley and Kelinfelder in [36, 37] and have been extensively studied since then [24, 34, 47, 48, 58, 61, 64, 65, 68, 69]. The underline mathematical model for the C-V technique is a one-dimensional drift-diffusion-Poisson system; see (6) below for a simplified multi-dimensional version. The main technique is based on the depletion approximation which allows one to build an explicit relation between the doping profile and the voltage-to-capacity data. The validity and accuracy of the depletion region approximation, however, have been always been questioned since the invention of the technology [34, 40, 46].

Mathematically, the doping profiling problem is an inverse problem of differential equations. The doping profile is parameterized as a function in a set of differential equations that describe the transport of charged particles and the distribution of electrical field inside semiconductor devices; see for example the equations in (1) and (6). The measurement that is available is usually a linear functional of the solutions of the differential equations; see for example (9) and (10) for the explicit definition of electric current that is measured. The objective is to reconstruct the doping function from the measurement. Those inverse problems related to semiconductor device modeling have been studied recently in the mathematics and computation community in recent years; see for example [3, 8, 22, 23, 28, 41, 42, 66, 67, 70].

Even though it is generally believed that the transport of charges in semiconductor devices is best modelled by the Boltzmann-Poisson system of equations, in the majority of recent research on semiconductor inverse problems, the mathematical model for charged particles transport have been chosen as the drift-diffusion-Poisson system [8, 41, 42, 67], a simplified model of Boltzmann-Poisson transport system. The reason for using this simplified model is because it is mathematically more convenient to analyze and computationally less expensive to solve. The drift-diffusion-Poisson approximation is valid in specific situations, mainly when the device is large compared to the mean free path of the electrons and the applied potential is weak. For devices of small size, with strong applied potential, it has been shown that current-voltage characteristics simulated with the Boltzmann-Poisson model and those with drift-diffusion-Poisson model can be significantly different [11]. On the other hand, how will this difference play a role in the reconstruction is still unknown. The main objective of this paper is exactly to study numerically reconstruction problems for the more accurate Boltzmann-Poisson model and to characterize the difference between reconstructions obtained with the BP model and those obtained with the DDP model. To the best of our knowledge, the only work related to inverse doping problem in the literature that goes beyond the drift-diffusion-Poisson model is reference [21] where the energy transport model is adopted.

The rest of the paper is organized as follows. In Section 2 we introduce the Boltzmann-Poisson model of electron transport in semiconductor devices. We also present its drift-diffusion-Poisson approximation. In Section 3 we formulate the inverse problem mathematically and remark briefly some basic properties of the inverse problems. We introduce in

Section 4 numerical procedures that are based on numerical minimization methods to solve the inverse doping problem and detail some numerical issues in Section 5 on the implementation of the algorithms. Detailed numerical reconstruction results based on synthetic data as well as some comparison between Boltzmann-Poisson reconstruction and drift-diffusion-Poisson reconstruction are presented in Section 6. Conclusions and further remarks are offered in Section 7.

2 The Boltzmann-Poisson system

We denote by $\Omega \subset \mathbb{R}^d$ $(d \geq 1)$ the spatial domain of interest (i.e. the device) and $\partial\Omega$ its boundary. Denote by $\mathbb{R}_+ = (0,\ \infty)$ the time axis. The transport of electrons in the semiconductor device is well modelled by the Boltzmann-Poisson system, which in semi-classical regime can be written as

$$\begin{aligned} \partial_t f + \mathbf{v}(\mathbf{k}) \cdot \nabla_{\mathbf{x}} f + \frac{q}{\hbar} \nabla_{\mathbf{x}} \Phi \cdot \nabla_{\mathbf{k}} f &= Q(f), && \text{in } \mathbb{R}_+ \times \Omega \times \mathbb{R}^d \\ -\nabla_{\mathbf{x}} \cdot (\epsilon(\mathbf{x}) \nabla_{\mathbf{x}} \Phi) &= \frac{q}{\epsilon_0}[\mathcal{N}(\mathbf{x}) - n], && \text{in } \mathbb{R}_+ \times \Omega \end{aligned} \tag{1}$$

where $f(t, \mathbf{x}, \mathbf{k})$ is the probability density function (pdf) of the electrons, $\hbar$ is the Planck constant divided by 2π, and q the positive electric charge. The constant ϵ_0 is the dielectric constant in vacuum and the function $\epsilon(\mathbf{x})$ is the relative dielectric function. The density of the electrons is defined as $n(t, \mathbf{x}) = \int_{\mathbb{R}^d} f(t, \mathbf{x}, \mathbf{k}) d\mathbf{k}$. The function $\mathcal{N}(\mathbf{x})$ is the doping profile. The energy band function $\mathcal{E}(\mathbf{k})$ describes the relation between energy and wavevector $\mathbf{k}$ so that the velocity of the electrons in the band can be written as $\mathbf{v} = \frac{1}{\hbar} \nabla_{\mathbf{k}} \mathcal{E}(\mathbf{k})$. In this work, we are interested in the so-called parabolic regime where $\mathcal{E}(\mathbf{k})$ is expressed as:

$$\mathcal{E}(\mathbf{k}) = \frac{\hbar^2 |\mathbf{k}|^2}{2 m_*}, \text{ in which case, } \mathbf{v}(\mathbf{k}) = \frac{\hbar \mathbf{k}}{m_*}$$

with m_* the effective mass of the electron in the crystal lattice. Note that since $\mathbf{v}(\mathbf{k})$ is independent of $\mathbf{x}$ and Φ is independent of $\mathbf{x}$, the transport terms (the second and third term on the left-hand-side of the first equation) can be written in conservative form as $\nabla_{\mathbf{x}} \cdot (\mathbf{v}(\mathbf{k}) f) + \nabla_{\mathbf{k}} \cdot (\frac{q}{\hbar} \nabla_{\mathbf{x}} \Phi f)$ so that the whole system is in conservative form.

We consider the case of low-density approximations so that we can have linear scattering term. The scattering operators Q takes the form:

$$Q(f)(t, \mathbf{x}, \mathbf{k}) = \int_{\mathbb{R}^d} \Big[\mathcal{K}(\mathbf{k}', \mathbf{k}) f(t, \mathbf{x}, \mathbf{k}') - \mathcal{K}(\mathbf{k}, \mathbf{k}') f(t, \mathbf{x}, \mathbf{k}) \Big] d\mathbf{k}', \tag{2}$$

where the scattering kernel $\mathcal{K}(\mathbf{k}, \mathbf{k}')$ denotes the space-dependent scattering rate which is chosen to be

$$\mathcal{K}(\mathbf{k}, \mathbf{k}') = \sum_{\alpha \in \{+,0,-\}} a_\alpha \delta(\mathcal{E}(\mathbf{k}) - \mathcal{E}(\mathbf{k}') + c_\alpha \hbar \omega_p), \tag{3}$$

with δ denoting the usual Dirac distribution, $(c_+,\ c_0,\ c_-) = (+1,\ 0,\ -1)$ and ω_p the constant phonon frequency. The constants $(a_+,\ a_0,\ a_-) = ((n_q+1)K,\ K_0,\ n_qK)$ with the occupation number of phonons $n_q = \left[\exp(\frac{\hbar\omega_p}{k_BT}) - 1\right]^{-1}$, and K_0, K are known constants. Here k_B is the Boltzmann constant, and T is the absolute temperature. Since the energy band function $\mathcal{E}$ depend only on the modulus of $\mathbf{k}$, we conclude that the scattering kernel is isotropic.

To impose boundary conditions for the Boltzmann-Poisson system (1), let us first recall the classical boundary sets of the phase space $\Omega \times \mathbb{R}^d$, $\Gamma_\pm$, defined as

$$\Gamma_\pm = \{(\mathbf{x}, \mathbf{k}) \in \partial\Omega \times \mathbb{R}^d \text{ s.t. } \pm \mathbf{v}(\mathbf{k}) \cdot \boldsymbol{\nu}(\mathbf{x}) > 0\}$$

with $\boldsymbol{\nu}(\mathbf{x})$ the unit outer normal vector at $\mathbf{x} \in \partial\Omega$. We assume that the boundary $\partial\Omega$ of the device splits into two disjoint parts $\partial\Omega_D$ and $\partial\Omega_N$, $\partial\Omega_D \cap \partial\Omega_N = \emptyset$ and $\partial\Omega = \partial\Omega_D \cup \partial\Omega_N$, where $\partial\Omega_D$ models the Ohmic contacts of the device and $\partial\Omega_N$ represents the insulating parts of the boundary. We can define similarly the boundary sets $\Gamma_\pm^D$ and $\Gamma_\pm^N$. We can now introduce the following boundary conditions for the Boltzmann-Poisson system (1):

$$\begin{array}{llll} f(t,\mathbf{x},\mathbf{k}) = f_D(t,\mathbf{x},\mathbf{k}) & \text{on } \mathbb{R}_+ \times \Gamma_-^D, & f(t,\mathbf{x},\mathbf{k}) = f(t,\mathbf{x},\mathbf{k}^*) & \text{on } \mathbb{R}_+ \times \Gamma_-^N, \\ \Phi(t,\mathbf{x}) = \varphi_D, & \text{on } \mathbb{R}_+ \times \partial\Omega_D, & \boldsymbol{\nu}(\mathbf{x}) \cdot \epsilon\nabla_{\mathbf{x}}\Phi = 0 & \text{on } \mathbb{R}_+ \times \partial\Omega_N, \end{array} \tag{4}$$

with f_D and φ_D given functions and the wave vector $\mathbf{k}^*$ satisfying the condition: $\mathbf{v}(\mathbf{k}^*) = \mathbf{v}(\mathbf{k}) - 2(\boldsymbol{\nu}(\mathbf{x})\cdot\mathbf{v})\boldsymbol{\nu}$. This means that specular reflection happens on the insulating boundary.

The initial condition for the Boltzmann-Poisson system is only needed for the f-component of the system

$$f(t,\mathbf{x},\mathbf{k}) = f_0(\mathbf{x},\mathbf{k}), \qquad \text{in } \{0\} \times \Omega \times \mathbb{R}^d. \tag{5}$$

The initial condition of the system does not play a crucial role in the study of the inverse problems that we are interested in. In this work, we take the initial condition to be a local Maxwellian distribution at the lattice temperature normalized so that the initial density $n(0,\mathbf{x})$ is equal to the chosen doping profile.

The Boltzmann-Poisson system (1) is very complicated to analyze mathematically and very expensive to solve numerically. It is thus often preferable to replace the system with the so-called drift-diffusion-Poisson approximation. To be more precise, let us denote by $\mathcal{E}_T = k_BT$ the thermal energy and $v_* = \sqrt{\dfrac{2\mathcal{E}_T}{m_*}}$ the characteristic speed associated with $\mathcal{E}_T$. Denote by $\tau(\mathbf{k}) = \Big(\displaystyle\int_{\mathbb{R}^d} \mathcal{K}(\mathbf{k},\mathbf{k}')d\mathbf{k}'\Big)^{-1}$ the relaxation time, i.e. average time between two successive collisions at wavevector $\mathbf{k}$, then the mean free path of the electrons is defined as $l(\mathbf{k}) = \tau v_*$. Denote by L the characteristic length of the device and $[\Phi]$ the maximum potential drop across the device. Let us define the nondimensionalized parameter $\varepsilon = l/L$. It can then be shown that, if $[\Phi]$ is on the order of thermal voltage $V_T = \mathcal{E}_T/q$, i.e. $[\Phi] \sim O(V_T)$, then in the limit of $\varepsilon \to 0$, i.e., when electrons undergo many collisions along their way through the device, the electron density n and potential Φ solve the following drift-diffusion-Poisson system:

$$\begin{aligned} \partial_t n + \nabla \cdot (-\mathcal{D}\nabla_{\mathbf{x}} n + \mu n \nabla_{\mathbf{x}}\Phi) &= 0, && \text{in } \mathbb{R}_+ \times \Omega \\ -\nabla_{\mathbf{x}} \cdot (\epsilon\nabla_{\mathbf{x}}\Phi) &= \frac{q}{\epsilon_0}[\mathcal{N}(\mathbf{x}) - n], && \text{in } \mathbb{R}_+ \times \Omega, \end{aligned} \tag{6}$$

where the coefficients $\mathcal{D}$ and μ are called the diffusivity and the mobility, respectively. They can be computed using the parameters in the Boltzmann-Poisson system. To keep the flow of the presentation, we postpone the calculation of those parameters to Section 5.2.

The boundary and initial conditions for the drift-diffusion-Poisson model that correspond to (4) and (5) can be written, respectively, as

$$\begin{array}{llll} n(t,\mathbf{x}) = n_D(t,\mathbf{x}) & \text{on} \ \ \mathbb{R}_+ \times \partial\Omega_D, & \boldsymbol{\nu}\cdot\mathcal{D}\nabla_{\mathbf{x}} n(t,\mathbf{x}) = 0 & \text{on} \ \ \mathbb{R}_+ \times \partial\Omega_N, \\ \Phi(t,\mathbf{x}) = \varphi_D, & \text{on} \ \ \mathbb{R}_+ \times \partial\Omega_D, & \boldsymbol{\nu}\cdot\epsilon\nabla_{\mathbf{x}}\Phi = 0 & \text{on} \ \ \mathbb{R}_+ \times \partial\Omega_N, \end{array} \tag{7}$$

and

$$n(t,\mathbf{x}) = n_0(\mathbf{x}), \qquad \text{in} \ \ \{0\}\times\Omega. \tag{8}$$

The functions n_D and n_0 are the averages of the functions f_D and f_0, respectively, over the $\mathbf{k}$ variable.

For the derivation of the drift-diffusion-Poisson models from the Boltzmann-Poisson system, we refer interested reader to the monographs [4, 35, 44]. The scattering kernel $\mathcal{K}$ that we have adopted in this paper is inelastic and thus is not symmetric with respect to the $\mathbf{k}$ and $\mathbf{k}'$ variable. The derivation of drift-diffusion-Poisson model for this type of kernel are presented in [20, 45, 57] under more general circumstances.

As we have remarked above, the drift-diffusion-Poisson approximation is accurate in many cases when the size of the device is sufficiently large ($> 1\ \mu m$ usually) compared to the mean free path of the electrons, and the electric field is relatively weak ($\ll 1\ V$) inside the device. The approximation breaks down in opposite situations. With recent advances in nanoscale devices, there are considerable interests in going beyond the drift-diffusion-Poisson model. That's one of the motivation of the current study. For the applications of different models in semiconductor modeling, we refer to [4, 7, 11, 13, 14, 15, 16, 32, 33, 44, 59, 60] and references therein.

We remark finally that the models we consider here are called unipolar models because we only consider the transport of electrons while neglected the transport of holes. Also, in real device simulation, both the Boltzmann-Poisson equation system and its boundary conditions can be more complicated than what we have presented here; see for example the above-mentioned references and [18, 25, 33, 54].

3 Inverse Problems

Even though the existence and uniqueness of solution to initial value problems of the nonlinear Boltzmann-Poisson system have been established in [49] in the whole space, the existence and uniqueness questions for the initial boundary value problem (1), (4) and (5), are largely open. The only result that we know is [1] where the existence of weak solutions to Boltzmann-Poisson system in 1×1 phase-space dimension is established with incoming data with polynomial decay. Extensive numerical studies in the past have, however, showed that the system, in higher dimension, does admit a unique solution with reasonable initial and boundary data; see for example [14, 17, 18] and references therein. We thus assume here that existence and uniqueness of solutions hold.

3.1 Full nonlinear case

We are interested in doping profiling problems with I-V data. We define the electric current through the boundary $\partial\Omega_D$ as:

$$\mathcal{I}(\varphi_D) = \int_{B_{\mathbf{x}}^+} \mathbf{v}(\mathbf{k}) \cdot \boldsymbol{\nu}(\mathbf{x}) f|_{\partial\Omega_D} d\mathbf{k}, \tag{9}$$

where $B_{\mathbf{x}}^+$ is the set of wave vectors defined as $B_{\mathbf{x}}^+ = \{\mathbf{k} \in \mathbb{R}^d : \mathbf{v}(\mathbf{k}) \cdot \boldsymbol{\nu}(\mathbf{x}) > 0\}$. The corresponding current for the drift-diffusion-Poisson model is

$$\mathcal{I}(\varphi_D) = \boldsymbol{\nu}(\mathbf{x}) \cdot (-\mathcal{D}\nabla_{\mathbf{x}} n + \mu n \nabla_{\mathbf{x}} \Phi)|_{\partial\Omega_D}. \tag{10}$$

Note that since the current through the boundary depends on the boundary voltage applied, we have explicitly indicated this dependence in the above definitions.

We have thus constructed a map between boundary applied voltage and boundary electric current:

$$\Lambda_t : \varphi_D \mapsto \mathcal{I}, \qquad t \in \mathbb{T}, \tag{11}$$

where $\mathbb{T} = (0,\ t_{\max})$ is the time interval on which measurements are taken. The map is similar to Dirichlet-to-Neumann maps in the theory of elliptic PDEs. The map Λ_t is nonlinear because the Boltzmann-Poisson (resp. drift-diffusion-Poisson) system is nonlinear. The map Λ_t clearly depends on the doping profile $\mathcal{N}$ in the Boltzmann-Poisson (resp. drift-diffusion-Poisson). If we are provided with the doping profile and other necessary parameters for the Boltzmann-Poisson system, then we can construct the map Λ_t by solving the systems for different applied voltages. Here we are interested in the inverse problem. That is, suppose we can measure data given in the map Λ_t, i.e., for each boundary applied voltage φ_D, we can measure the boundary electric current $\mathcal{I}(\varphi_D)$, we want to recover the doping profile function $\mathcal{N}(\mathbf{x})$ from these measurements. This doping profile reconstruction problem can be formulated as follows.

Inverse Doping Problem (IDP). *To reconstruct the doping profile function $\mathcal{N}(\mathbf{x})$ in the Boltzmann-Poisson (resp. the drift-diffusion-Poisson) system from measured voltage-to-current map Λ_t defined in (11) with current of the form (9) (resp. (10)).*

The inverse doping problem is a highly nonlinear inverse problem because the voltage-to-current map Λ_t is a nonlinear functional of the doping profile $\mathcal{N}(\mathbf{x})$. Moreover, the forward models, either the Boltzmann-Poisson system or the drift-diffusion-Poisson system, are nonlinear systems for given doping profiles. Due to its analytical and computational advantages, past studies on the inverse problems have focused on the drift-diffusion-Poisson model (6); see for example [8, 9, 21, 28]. Both time-dependent and stationary data have been considered [8, 41, 67]. As we have pointed out, current developments in nanoscale semiconductor devices have demonstrated that it is necessary now to use the more accurate Boltzmann-Poisson model for device simulation [11]. The identification problems for the Boltzmann-Poisson model, however, have not been studied to the best of our knowledge, although inverse problems related to other linear transport models have been extensively studied in recent years; see for example [6] for recent reviews on analytical aspect and [38,

39, 52] for numerical aspect of nonlinear inverse problems related to the transport equation. This is the main motivation for the current study of the inverse problem.

The fact that analytical results on the inverse problem are too difficult to obtain forces us to resort to numerical methods in this study. Our main objective is (i) to show numerically that the reconstruction of the doping profile is possible when appropriate *a prior* information is available and (ii) to show numerically that the reconstructions in transport regime using the Boltzmann-Poisson system are indeed more accurate than the reconstructions with the drift-diffusion-Poisson system. The assumption we made for (ii) to be true is that the physical process that generated the measured data is accurately modeled by the Boltzmann-Poisson system. However, as we will show in Section 6, the reconstructions with the Boltzmann-Poisson system is significantly slower than those with the drift-diffusion-Poisson system.

Computationally, the nonlinear inverse doping problems are solved by reformulating them into optimization problems. We attempt to minimize the discrepancy between model predictions and measurements. More precisely, we look for the doping profile function $\mathcal{N}(\mathbf{x})$ that minimizes the mismatch functional

$$\mathcal{F}(f_1, \cdots, f_s, \cdots, f_{N_S}, \mathcal{N}) = \frac{1}{2} \sum_{s=1}^{N_S} \int_{\mathbb{T}} \int_{\partial\Omega_D} \left(\mathcal{I}_s(\varphi_D^s) - \mathcal{I}_s^*\right)^2 d\sigma(\mathbf{x}) dt + \beta \mathcal{R}(\mathcal{N}), \tag{12}$$

where $d\sigma$ denotes the surface measure on $\partial\Omega_D$. The subscript s is used to denote quantities coming from the s-th applied voltage and N_S is the total number of voltages applied. The measurement data is denoted by $\mathcal{I}_s^*$. Let us emphasize here that although the function $\mathcal{N}$ does not appear explicitly in the first term of the above functional (12), it does enter through f_s.

The second term in functional is a regularization term, with β the regularization strength. In the past, both Tikhonov regularization and total variation regularization strategies have been used in inverse transport problems [26, 27, 52] and the strength of regularization is usually determined either by empirical cross validation or by the so-called L-curve method [62, 63]. In this paper, we will use a different regularization strategy, i.e., regularization by parameterization. We postpone further discussion to Section 5.3.

When the original inverse problem has a unique solution, the global minimizer of the objective functional (12) is the solution to the inverse problem. The difficulty in minimizing (12) lies in the fact that the functional is in general highly non-convex. There are thus multiple minimizers. Also, the unknown to be recovered, the doping profile $\mathcal{N}$, is an infinite-dimensional object, a function of space. This means that we have to deal with a large number of optimization variables when solving the problem numerically.

The mismatch functional we selected here is the L^2 norm of difference between measure current data and current data predicted by the Boltzmann-Poisson model. We are aware of the fact that when the measured data is noisy-free, L^1 norm may be a more physically-relevant norm to use. For the study initialized in this paper, we focus on the L^2 case for its computational simplicity. Detail discussions and comparison of the results with the two different norms will be presented elsewhere.

3.2 Linearized case

The nonlinear inverse problem we have just formulated is difficult to deal with. We now look at a simplified version of the reconstruction problem. We linearize the inverse problem around some known background doping profile $\mathcal{N}^0$ to obtain a linear inverse problem. We assume that we know the doping profile is

$$\mathcal{N} = \mathcal{N}^0 + \tilde{\mathcal{N}} \tag{13}$$

where $\tilde{\mathcal{N}}$ is small (in appropriate norm) compared to $\mathcal{N}_0$. Then the solution of the system can thus also be, formally, written as

$$f = f^0 + \tilde{f}, \qquad \Phi = \Phi^0 + \tilde{\Phi}, \tag{14}$$

where f^0 and Φ^0 are solutions of the Boltzmann-Poisson system (1) with background doping profile $\mathcal{N}^0$. This assumption is in general valid as observed from previous numerical simulations. The solution depends on doping profile in a continuous way unless we are in the runaway regime. It is then easy to show formally that $(\tilde{f}, \tilde{\Phi})$ solves, up to a high order correction, the following equation

$$\begin{aligned} \partial_t \tilde{f} + \mathbf{v}(\mathbf{k}) \cdot \nabla_{\mathbf{x}} \tilde{f} + \frac{q}{\hbar} \nabla_{\mathbf{x}} \tilde{\Phi} \cdot \nabla_{\mathbf{k}} f^0 + \frac{q}{\hbar} \nabla_{\mathbf{x}} \Phi^0 \cdot \nabla_{\mathbf{k}} \tilde{f} &= Q(\tilde{f}), && \text{in } \mathbb{T} \times \Omega \times \mathbb{R}^d \\ -\nabla_{\mathbf{x}} \cdot (\epsilon(\mathbf{x}) \nabla_{\mathbf{x}} \tilde{\Phi}) &= \frac{q}{\epsilon_0} [\tilde{\mathcal{N}}(\mathbf{x}) - \tilde{n}], && \text{in } \mathbb{T} \times \Omega \end{aligned} \tag{15}$$

with boundary and initial conditions given by

$$\begin{array}{llll} \tilde{f}(t, \mathbf{x}, \mathbf{k}) = 0 & \text{on } \mathbb{T} \times \Gamma_-^D, & \tilde{f}(t, \mathbf{x}, \mathbf{k}) = \tilde{f}(t, \mathbf{x}, \mathbf{k}^*) & \text{on } \mathbb{T} \times \Gamma_-^N, \\ \tilde{\Phi}(t, \mathbf{x}) = 0, & \text{on } \mathbb{T} \times \partial\Omega_D, & \boldsymbol{\nu}(\mathbf{x}) \cdot \epsilon \nabla_{\mathbf{x}} \tilde{\Phi} = 0 & \text{on } \mathbb{T} \times \partial\Omega_N, \\ \tilde{f}(0, \mathbf{x}, \mathbf{k}) = 0, & \text{in } \Omega \times \mathbb{R}^d & & \end{array} \tag{16}$$

The problem now is to reconstruct $\tilde{\mathcal{N}}$ from measurement

$$\tilde{\mathcal{I}}(\varphi_D) = \int_{B_{\mathbf{x}}^+} \mathbf{v}(\mathbf{k}) \cdot \boldsymbol{\nu}(\mathbf{x}) \tilde{f}|_{\partial\Omega_D} d\mathbf{k}, \qquad t \in \mathbb{T} \tag{17}$$

It is easy to see that the problem is now linear because the solution $\tilde{f}$ of (15) (thus the current in (17)) depends on $\tilde{N}$ in a linear way.

The linearized problem can be solved as follows. Let (g, Ψ) be the solution of the following adjoint problem

$$\begin{aligned} -\partial_t g - \mathbf{v}(\mathbf{k}) \cdot \nabla_{\mathbf{x}} g - \frac{q}{\hbar} \nabla_{\mathbf{x}} \Phi^0 \cdot \nabla_{\mathbf{k}} g &= Q(g) + \frac{q}{\epsilon_0} \Psi, && \text{in } \mathbb{T} \times \Omega \times \mathbb{R}^d \\ -\nabla_{\mathbf{x}} \cdot (\epsilon(\mathbf{x}) \nabla_{\mathbf{x}} \Psi) &= -\frac{q}{\hbar} \nabla_{\mathbf{k}} f^0 \cdot \nabla_{\mathbf{x}} g, && \text{in } \mathbb{T} \times \Omega \end{aligned} \tag{18}$$

with boundary and *final* conditions given by

$$\begin{array}{llll} g(t, \mathbf{x}, \mathbf{k}) = -\delta(\mathbf{x} - \mathbf{y}), & \text{on } \mathbb{T} \times \Gamma_+^D, & g(t, \mathbf{x}, \mathbf{k}) = 0 & \text{on } \mathbb{T} \times \Gamma_\pm^N, \\ \Psi(t, \mathbf{x}) = 0, & \text{on } \mathbb{T} \times \partial\Omega_D, & \boldsymbol{\nu}(\mathbf{x}) \cdot \epsilon \nabla_{\mathbf{x}} \Psi = 0 & \text{on } \mathbb{T} \times \partial\Omega_N, \\ g(t_{\max}, \mathbf{x}, \mathbf{k}) = 0, & \text{in } \Omega \times \mathbb{R}^d & & \end{array} \tag{19}$$

It is important to note that the boundary conditions for g is now posed on $\Gamma_+^D \cup \Gamma_\pm^N$ due to reciprocity. Besides, the adjoint system evolves backward in time from $t_{\max}$ to 0, thus the final condition is given instead of the initial condition.

One can then check, using integration by parts and the assumption that $\lim_{|\mathbf{k}|\to\infty} g(t,\mathbf{x},\mathbf{k}) = 0$, that

$$\int_\Omega \Big(\frac{q}{\epsilon_0}\int_{\mathbb{T}} \Psi(t,\mathbf{x};\mathbf{y})dt\Big)\tilde{\mathcal{N}}(\mathbf{x})d\mathbf{x} = \int_{\mathbb{T}} \tilde{\mathcal{I}}(\mathbf{y})dt. \tag{20}$$

This is linear map between the unknown $\tilde{\mathcal{N}}$ and the (time averaged) measured data. The kernel of the map, $\int_{\mathbb{T}} \Psi(t,\mathbf{x})dt$, is known. It remains to solve (20) to reconstruct the unknown $\tilde{\mathcal{N}}$. More details on the reconstruction procedure is presented in Section 4.3.

Let us conclude Section 3 by the following remark. The Boltzmann-Poisson system (1) is a system of nonlinear evolution equations. The solution of the system depends the boundary potential applied in a nonlinear way. In choosing applied potential, we have to make sure that the solution of the problem does not blow up under this applied potential. We thus have a small range of φ_D that we can use in practice. This fact limits the amount of data that we can collect for the solution of the reconstruction problems.

4 Reconstruction Methods

We now present the numerical method we used to solve the inverse problems we just formulated in the previous section. Our main interest is to solve the nonlinear inverse problems by solving the following constrained minimization problem:

$$\min_{f_1,\cdots,f_s,\cdots,f_{N_S},\mathcal{N}} \mathcal{F}(f_1,\cdots,f_s,\cdots,f_{N_S},\mathcal{N}) \tag{21}$$

subject to, $1 \le s \le N_S$,

$$\begin{aligned}
\partial_t f_s + \mathbf{v}(\mathbf{k})\cdot\nabla_{\mathbf{x}} f_s + \frac{q}{\hbar}\nabla_{\mathbf{x}}\Phi_s\cdot\nabla_{\mathbf{k}} f_s &= Q(f_s), \quad \text{in } \mathbb{T}\times\Omega\times\mathbb{R}^d \\
-\nabla_{\mathbf{x}}\cdot(\epsilon(\mathbf{x})\nabla_{\mathbf{x}}\Phi_s) &= \frac{q}{\epsilon_0}[\mathcal{N}(\mathbf{x}) - n_s], \quad \text{in } \mathbb{T}\times\Omega \\
f_s(t,\mathbf{x},\mathbf{k}) = f_D(t,\mathbf{x},\mathbf{k}) \quad \text{on } \mathbb{T}\times\Gamma_-^D, &\qquad f_s(t,\mathbf{x},\mathbf{k}) = f_s(t,\mathbf{x},\mathbf{k}^*) \quad \text{on } \mathbb{T}\times\Gamma_-^N, \\
\Phi_s(t,\mathbf{x}) = \varphi_D^s, \quad \text{on } \mathbb{T}\times\partial\Omega_D, &\qquad \boldsymbol{\nu}(\mathbf{x})\cdot\epsilon\nabla_{\mathbf{x}}\Phi_s = 0 \quad \text{on } \mathbb{T}\times\partial\Omega_N, \\
f_s(0,\mathbf{x},\mathbf{k}) = f_0(\mathbf{x},\mathbf{k}), \quad \text{in } \Omega\times\mathbb{R}^d.
\end{aligned} \tag{22}$$

where φ_D^s is the s-th applied potential while the incoming electron flux f_D is fixed for all cases.

4.1 Quasi-Newton method

There are many ways to solve this PDE-constrained minimization problem. For example, one can adopt the method of Lagrange multipliers such as those in [2, 29]. Here we solve the problem by transforming it into an unconstrained problem. The procedure is as follows. We eliminate the constraints by first solving the Boltzmann-Poisson system to obtain the relations $f_s = f_s(\mathcal{N}),\ 1 \le s \le N_S$. We then put these relations into the objective functional so that

the mismatch is now only functional of $\mathcal{N}$, $\tilde{\mathcal{F}}(\mathcal{N}) = \mathcal{F}(f_1(\mathcal{N}), \cdots, f_s(\mathcal{N}), \cdots, f_{N_S}(\mathcal{N}), \mathcal{N})$. We thus just need to minimize $\tilde{\mathcal{F}}(\mathcal{N})$ to obtain the solution of the inverse problem.

The minimization problem is solved by a quasi-Newton method. The method requires the computation of the gradient of the objective function with respective to the unknown $\mathcal{N}$. This is done by the adjoint state method. As before, we denote by (g_s, Ψ_s) the adjoint variables corresponding to (f_s, Φ_s), that solve the adjoint equations, $1 \leq s \leq N_S$:

$$\begin{aligned} -\partial_t g_s - \mathbf{v}(\mathbf{k}) \cdot \nabla_{\mathbf{x}} g_s - \frac{q}{\hbar} \nabla_{\mathbf{x}} \Phi_s \cdot \nabla_{\mathbf{k}} g_s &= Q(g_s) + \frac{q}{\epsilon_0} \Psi_s, \quad \text{in } \mathbb{T} \times \Omega \times \mathbb{R}^d \\ -\nabla_{\mathbf{x}} \cdot (\epsilon(\mathbf{x}) \nabla_{\mathbf{x}} \Psi_s) &= -\frac{q}{\hbar} \nabla_{\mathbf{k}} f_s \cdot \nabla_{\mathbf{x}} g_s, \quad \text{in } \mathbb{T} \times \Omega \end{aligned} \tag{23}$$

with boundary and *final* conditions given by

$$\begin{array}{llll} g_s(t, \mathbf{x}, \mathbf{k}) = -\mathbf{v}(\mathbf{k}) \cdot \boldsymbol{\nu}(\mathbf{x})(\mathcal{I}_s - \mathcal{I}_s^*), & \text{on } \mathbb{T} \times \Gamma_+^D, & g_s(t, \mathbf{x}, \mathbf{k}) = 0 & \text{on } \mathbb{T} \times \Gamma_\pm^N, \\ \Psi_s(t, \mathbf{x}) = 0, & \text{on } \mathbb{T} \times \partial\Omega_D, & \boldsymbol{\nu}(\mathbf{x}) \cdot \epsilon \nabla_{\mathbf{x}} \Psi_s = 0 & \text{on } \mathbb{T} \times \partial\Omega_N, \\ g_s(t_{\max}, \mathbf{x}, \mathbf{k}) = 0, & \text{in } \Omega \times \mathbb{R}^d & & \end{array} \tag{24}$$

Here in the adjoint equation (23), the variables f_s and Φ_s are solutions of the Boltzmann-Poisson system with the s-th applied potential. Note that the solution of the s-th adjoint problem depends only on the solution of the s-th forward problem, not the other $N_S - 1$ forward problems. We can then show that the Fréchet derivative of the objective function $\tilde{\mathcal{F}}(\mathcal{N})$ with respect to $\mathcal{N}$, when applied to perturbation h, can be written as

$$\tilde{\mathcal{F}}'(\mathcal{N})h = \frac{q}{\epsilon_0} \sum_{s=1}^{N_S} \int_\Omega \Big(\int_{\mathbb{T}} \Psi_s(t, \mathbf{x}) dt \Big) h(\mathbf{x}) d\mathbf{x} + \beta \int_\Omega \mathcal{R}'(\mathcal{N}) h(\mathbf{x}) d\mathbf{x}. \tag{25}$$

The same procedure can be employed to calculate the gradient of the objective functional with respect to the doping profile in the drift-diffusion-Poisson formulation. In this case, the adjoint problems read, still denoting by (η_s, Ψ_s) the adjoint variables, $1 \leq s \leq N_S$,

$$\begin{aligned} -\partial_t \eta_s - \nabla \cdot \mathcal{D} \nabla_{\mathbf{x}} \eta_s - \mu \nabla_{\mathbf{x}} \Phi_s \cdot \nabla \eta_s &= \frac{q}{\epsilon_0} \Psi_s, \quad \text{in } \mathbb{T} \times \Omega \\ -\nabla_{\mathbf{x}} \cdot (\epsilon \nabla_{\mathbf{x}} \Psi_s) &= \nabla_{\mathbf{x}} \cdot \mu n_s \nabla_{\mathbf{x}} \eta_s, \quad \text{in } \mathbb{T} \times \Omega. \end{aligned} \tag{26}$$

with the boundary and *final* conditions

$$\begin{array}{llll} \eta_s(t, \mathbf{x}) = -(\mathcal{I}_s - \mathcal{I}_s^*) & \text{on } \mathbb{T} \times \partial\Omega_D, & \boldsymbol{\nu} \cdot \nabla \eta_s(t, \mathbf{x}) = 0 & \text{on } \mathbb{T} \times \partial\Omega_N, \\ \Psi_s(t, \mathbf{x}) = 0, & \text{on } \mathbb{T} \times \partial\Omega_D, & \boldsymbol{\nu} \cdot \epsilon \nabla_{\mathbf{x}} \Psi_s = 0 & \text{on } \mathbb{T} \times \partial\Omega_N, \\ \eta_s(t_{\max}, \mathbf{x}) = 0, & \text{on } \Omega. & & \end{array} \tag{27}$$

The Fréchet derivative of the objective functional takes the same form as in (25), except that the Ψ_s ($1 \leq s \leq N_S$) is now the solution of the drift-diffusion-Poisson system with applied potential φ_D^s.

Once we are able to compute the gradient of the objective functional with respect to the change of the unknowns, we use the quasi-Newton method with BFGS rule to update the Hessian operator. The method is classical so we would not present the details here but refer interested reader to [52, 53] for the application of the method in other inverse transport calculations.

4.2 Iterative quasi-Newton method

In the quasi-Newton method we just described, we linearize the inverse problem at each Newton iteration. The forward model we have to deal with is the nonlinear Boltzmann-Poisson system. We now propose a slightly different scheme for the reconstruction. The method is based on the observation that the measurement is taken on only the f-component of the system. We observe that if we linearize the forward problem by fixing the density in the Poisson equation, we reduce the reconstruction problem to an inverse coefficient problem, still nonlinear though, for the linearized transport equation. The method starts with an initial guess $\mathcal{N}^0$. To obtain initial guesses for the density functions, we solve the following linearized problem, $1 \le s \le N_S$,

$$\begin{aligned} \partial_t f_s + \mathbf{v}(\mathbf{k}) \cdot \nabla_{\mathbf{x}} f_s + \frac{q}{\hbar} \nabla_{\mathbf{x}} \Phi \cdot \nabla_{\mathbf{k}} f_s &= Q(f_s), \quad \text{in } \mathbb{T} \times \Omega \times \mathbb{R}^d \\ -\nabla_{\mathbf{x}} \cdot (\epsilon(\mathbf{x}) \nabla_{\mathbf{x}} \Phi) &= \frac{q}{\epsilon_0} \mathcal{N}^0, , \quad \text{in } \mathbb{T} \times \Omega \times \mathbb{R}^d \end{aligned}$$

using the same boundary and initial conditions as those in the original nonlinear problem. The reconstruction procedure then proceeds as follows. At iteration k, we solve the inverse problem with measured data using the following linearized model to find $(\mathcal{N}^k, \{f_s^k\}_{s=1}^{N_S})$

$$\min_{f_1, \cdots, f_s, \cdots, f_{N_S}, \mathcal{N}} \mathcal{F}(f_1, \cdots, f_s, \cdots, f_{N_S}, \mathcal{N}) \tag{28}$$

subject to, $1 \le s \le N_S$,

$$\begin{aligned} \partial_t f_s + \mathbf{v}(\mathbf{k}) \cdot \nabla_{\mathbf{x}} f_s + \frac{q}{\hbar} \nabla_{\mathbf{x}} \Phi_s \cdot \nabla_{\mathbf{k}} f_s &= Q(f_s), \quad \text{in } \mathbb{T} \times \Omega \times \mathbb{R}^d \\ -\nabla_{\mathbf{x}} \cdot (\epsilon(\mathbf{x}) \nabla_{\mathbf{x}} \Phi_s) &= \frac{q}{\epsilon_0} [\mathcal{N}(\mathbf{x}) - n_s^{k-1}], \quad \text{in } \mathbb{T} \times \Omega \end{aligned}$$

$$\begin{aligned} &f_s(t, \mathbf{x}, \mathbf{k}) = f_D(t, \mathbf{x}, \mathbf{k}) \quad \text{on } \mathbb{T} \times \Gamma_-^D, \qquad && f_s(t, \mathbf{x}, \mathbf{k}) = f_s(t, \mathbf{x}, \mathbf{k}^*) \quad \text{on } \mathbb{T} \times \Gamma_-^N, \\ &\Phi_s(t, \mathbf{x}) = \varphi_D^s, \quad \text{on } \mathbb{T} \times \partial\Omega_D, && \boldsymbol{\nu}(\mathbf{x}) \cdot \epsilon \nabla_{\mathbf{x}} \Phi_s = 0 \quad \text{on } \mathbb{T} \times \partial\Omega_N, \\ &f_s(0, \mathbf{x}, \mathbf{k}) = f_0(\mathbf{x}, \mathbf{k}), \quad \text{in } \Omega \times \mathbb{R}^d. \end{aligned}$$

The iteration continues until converges. The advantage of this iteration is that we only need to deal with linear forward problem at each iteration. However, this fixed point type of iteration converges slower in general than Newton type of iteration.

In each iteration, we need to solve the minimization problem (28). We can then use the quasi-Newton method that we presented in the previous section. To compute the Fréchet derivatives of the objective functional with respect to the unknown for this minimization problem, we can adopt the same strategy of adjoint equations. It turns out that the adjoint problems are almost identical to the adjoint problems in (23) and (24). To save spaces, we do not present those equations here.

4.3 Linearized reconstruction

To solve the linearized inverse problem, we first solve the Boltzmann-Poisson system with background doping profile $\mathcal{N}^0$ to get f^0 and Φ^0. We then put (f^0, Φ^0) in the adjoint equation (18) and solve the equation to obtain Ψ. We have thus constructed the kernel

of the integral equation (20). It remains to solve this integral equation to reconstruct the perturbation $\tilde{\mathcal{N}}$.

Let us assume that we discretize $\tilde{\mathcal{N}}$ on a spatial mesh of N_Ω nodes. Then, after collecting the discretization for all N_S applied potentials, we obtain a linear system of algebraic equation of the form

$$\mathcal{A}\tilde{\mathcal{N}} = \mathcal{Z}, \tag{29}$$

with the matrix $\mathcal{A}$ and the column vector $\mathcal{Z}$ of the form

$$\mathcal{A} = [\mathcal{A}_1^{\mathfrak{T}}, \cdots, \mathcal{A}_{N_S}^{\mathfrak{T}}]^{\mathfrak{T}} \qquad \mathcal{Z} = [\mathcal{Z}_1^{\mathfrak{T}}, \cdots, \mathcal{Z}_{N_S}^{\mathfrak{T}}]^{\mathfrak{T}}, \tag{30}$$

with $\mathcal{A}_s$ and $\mathcal{Z}_s$ the discretization of the integral and the measurement, respectively and the superscript $\mathfrak{T}$ denoting the transpose of a quantity. The $\tilde{\mathcal{N}}$ now denotes the column vector that contains the value of the function $\tilde{\mathcal{N}}$ on the mesh nodes.

It remains to solve (29) in regularized least-square sense to obtain $\tilde{\mathcal{N}}$. For example, when Tikhonov regularization is used, $\tilde{\mathcal{N}}$ is found as the solution to

$$\min_{\tilde{\mathcal{N}}} \frac{1}{2}\|\mathcal{A}\tilde{\mathcal{N}} - \mathcal{Z}\|_2^2 + \frac{\beta}{2}\|\tilde{\mathcal{N}}\|_2^2. \tag{31}$$

The minimizer of (31) is the solution of the normal equation

$$(\mathcal{A}^{\mathfrak{T}}\mathcal{A} + \beta\mathcal{I})\tilde{\mathcal{N}} = \mathcal{A}^{\mathfrak{T}}\mathcal{Z}, \tag{32}$$

that is

$$\tilde{\mathcal{N}} = (\mathcal{A}^{\mathfrak{T}}\mathcal{A} + \beta\mathcal{I})^{-1}\mathcal{A}^{\mathfrak{T}}\mathcal{Z}. \tag{33}$$

In practice, when the number of unknowns (discretized optical properties or sources) is large, the inverse matrix $(\mathcal{A}^{\mathfrak{T}}\mathcal{A} + \beta\mathcal{I})^{-1}$ is usually not formed directly. Instead, iterative methods are used to solve (32).

5 Implementation Issues

The reconstruction strategies that we have presented have to be realized with computation. We present here very briefly some issues related to the implementations, including the discretization of the Boltzmann-Poisson system using the discontinuous Galerkin method and the parameterization of the unknown doping profile function to reduce the ill-posedness of the inverse problem.

5.1 Numerical discretization

We have seen that in each Newton iteration of the reconstruction algorithms, we need to solve numerically the Boltzmann-Poisson system (1) and the adjoint problem (6) repeatedly over different applied potentials.

To deal with the delta function in the scattering kernel $\mathcal{K}(\mathbf{k}, \mathbf{k}')$, we first notice that $\mathcal{K}$ depend only on the modulus $|\mathbf{k}|$ and $|\mathbf{k}'|$. This allows us to integrate out the delta functions

in the scattering kernel by passing the scattering integral to the spherical coordinate using $d\mathbf{k}' = |\mathbf{k}'|^{d-1} d|\mathbf{k}'| d\hat{\mathbf{k}}'$ to obtain

$$Q^+(f) = \int_{\mathbb{R}^d} \sum_{\alpha\in\{+,0,-\}} a_\alpha \delta(\mathcal{E}(|\mathbf{k}'|) - \mathcal{E}(|\mathbf{k}|) + c_\alpha \hbar\omega_p) f(t,\mathbf{x},|\mathbf{k}'|\hat{\mathbf{k}}')|\mathbf{k}'|^{d-1} d|\mathbf{k}'| d\hat{\mathbf{k}}' \quad (34)$$

$$= \sum_{\alpha\in\{+,0,-\}} \frac{a_\alpha}{2} (\frac{\hbar^2}{2m_*})^{-1} \big(|\mathbf{k}|^2 - \tilde{c}_\alpha\big)^{\frac{d-2}{2}} \int_{\mathbb{S}^{d-1}} f(t,\mathbf{x},\sqrt{|\mathbf{k}|^2 - \tilde{c}_\alpha}\hat{\mathbf{k}}') d\hat{\mathbf{k}}' \quad (35)$$

and

$$Q^-(f) = \sum_{\alpha\in\{+,0,-\}} \frac{A_d a_\alpha}{2} (\frac{\hbar^2}{2m_*})^{-1} \big(|\mathbf{k}|^2 + \tilde{c}_\alpha\big)^{\frac{d-2}{2}} f(t,\mathbf{x},|\mathbf{k}|\hat{\mathbf{k}}), \quad (36)$$

where we have used the decomposition $\mathbb{R}^d = \mathbb{R}_+ \times \mathbb{S}^{d-1}$ with $\mathbb{S}^{d-1}$ the unit sphere in $\mathbb{R}^d$ and $A_d = \dfrac{2\pi^{d/2}}{\Gamma(d/2)}$ the surface area of $\mathbb{S}^{d-1}$, Γ being the usual Gamma function. The new constants $\tilde{c}_\alpha = (\dfrac{\hbar^2}{2m_*})^{-1} c_\alpha \hbar\omega_p$.

We now non-dimensionalize the Boltzmann-Poisson system using the scaling introduced in [12, 43]. We take the lattice temperature $T = 300\ K$ and introduce the following characteristic quantities: length $l_* = 10^{-6}\ m$, time $t_* = 10^{-12}\ s$, density $n^* = \max_{\mathbf{x}} \mathcal{N}$ and potential $\Phi_* = V_T\ V$, V_T being the thermal voltage. The thermal energy $\mathcal{E}_T$ induces a characteristic speed $v_* = \sqrt{\dfrac{2\mathcal{E}_T}{m_*}}$ which then induces a characteristic wavenumber $k_* = \dfrac{\sqrt{2m_* k_B T}}{\hbar}$. We can now introduce non-dimensionalized quantities by the following change of variables

$$\mathbf{x} \to l_*\mathbf{x}, \quad t \to t_* t, \quad \Phi \to \Phi_*\Phi, \quad \mathbf{k} \to k_*\mathbf{k}, \quad f \to n_* f. \quad (37)$$

and the rescaled Boltzmann-Poisson system reads,

$$\begin{aligned} \partial_t f + \nabla_{\mathbf{x}} \cdot (\vartheta_1 |\mathbf{k}| \hat{\mathbf{k}} f) + \nabla_{\mathbf{k}} \cdot \big(\vartheta_2 \nabla_{\mathbf{x}} \Phi f\big) &= Q_*(f), \\ -\nabla_{\mathbf{x}} \cdot (\lambda^2(\mathbf{x}) \nabla_{\mathbf{x}} \Phi) &= \mathcal{N}(\mathbf{x}) - n, \end{aligned} \quad (38)$$

where the nondimensionalized parameters are defined as $\vartheta_1 = \dfrac{\hbar k_* t_*}{l_* m_*}$, $\vartheta_2 = \dfrac{q\Phi_* t_*}{\hbar l_* k_*}$, and $\lambda = \dfrac{1}{l_*}\sqrt{\dfrac{\epsilon_0 \epsilon \Phi_*}{q n_*}}$ is the local rescaled Debye length. The scattering operator now reads,

$$Q_*(f) = \sum_{\alpha\in\{+,0,-\}} \mathcal{M}_\alpha^+ \int_{\mathbb{S}^{d-1}} f(t,\mathbf{x},k_*\sqrt{|\mathbf{k}|^2 - \tilde{c}_\alpha}\hat{\mathbf{k}}') d\hat{\mathbf{k}}' - A_d \mathcal{M}_\alpha^- f(t,\mathbf{x},k_*|\mathbf{k}|\hat{\mathbf{k}}),$$

with the constants $\mathcal{M}_\alpha^\pm = t_* \dfrac{a_\alpha}{2} (\dfrac{\hbar^2}{2m_*})^{-1} (k_*^2|\mathbf{k}|^2 \pm \tilde{c}_\alpha)^{\frac{d-2}{2}}$.

The rescaled Boltzmann-Poisson system (38) is intentionally written in conservative form so that it can be easily passed to a discontinuous Galerkin discretization strategy. In our

implementation, we focus on the three-dimensional case ($d = 3$) so that we can parameterize the direction variable $\hat{\mathbf{k}}$ by, with the abuse of the notations μ and φ,

$$\hat{\mathbf{k}} = (\mu, \sqrt{1-\mu^2}\cos\varphi, \sqrt{1-\mu^2}\sin\varphi). \tag{39}$$

Here μ is the cosine of the polar angle and φ is the azimuth angle. The divergence operator $\nabla_{\mathbf{k}}\cdot$ is now replaced with its equivalence in the spherical coordinate. To simplify the numerical computation, we also assume that the system we have is invariant in the $z-$direction so that the $\nabla_{\mathbf{x}} = (\partial_x, \partial_y, 0)$. We refer to [18] for details on the discretization of the Boltzmann-Poisson system with the discontinuous Galerkin scheme and some forward simulation results [18].

To discretize the adjoint problems, we employ the same strategy. Since the adjoint problems are backward evolution equations, i.e., final value problems, we first perform a change of variable $t \to t_{\max} - t$ to change the adjoint problems into usual initial value problems. For example, the adjoint problem in (23) is transformed to

$$\begin{aligned} \partial_t g - \mathbf{v}(\mathbf{k})\cdot\nabla_{\mathbf{x}} g - \frac{q}{\hbar}\nabla_{\mathbf{x}}\Phi^0\cdot\nabla_{\mathbf{k}} g &= Q(g) + \frac{q}{\epsilon_0}\Psi, \qquad \text{in } \mathbb{T}\times\Omega\times\mathbb{R}^d \\ -\nabla_{\mathbf{x}}\cdot(\epsilon(\mathbf{x})\nabla_{\mathbf{x}}\Psi) &= -\frac{q}{\hbar}\nabla_{\mathbf{k}} f^0\cdot\nabla_{\mathbf{x}} g, \quad \text{in } \mathbb{T}\times\Omega \end{aligned} \tag{40}$$

with initial condition $g(0, \mathbf{x}, \mathbf{k}) = 0$ and same boundary conditions as in (24). We then following the same procedure as we have described above and discretize using the discontinuous Galerkin method.

5.2 Diffusivity and mobility coefficients

We recall briefly here how the two coefficients are calculated. We first notices that because the two constants a_+ and a_- are different in (3), the scattering kernel adopted in this paper, $\mathcal{K}$, is not symmetric in the sense that $\mathcal{K}(\mathbf{k}, \mathbf{k}') \neq \mathcal{K}(\mathbf{k}', \mathbf{k})$. This means that the microscopic scattering process is not reversible. The classical ways to derive drift-diffusion-Poisson model from Boltzmann-Poisson model (1), such as those presented in [4, 35, 44] have to be modified to take into account this irreversibility effect. Following the presentation in [20, 45] but noticing that our scattering kernel is independent of the spatial variable $\mathbf{x}$, let us denote by $F(\mathbf{k})$ a function in the kernel of the scattering operator

$$Q(F) = 0, \quad \text{normalized in the sense that, } \int_{\mathbb{R}^d} F(\mathbf{k})d\mathbf{k} = 1. \tag{41}$$

We also introduce a vector function $\boldsymbol{\xi}(\mathbf{k})$ that solves

$$Q(\boldsymbol{\xi}) = \mathbf{v}(\mathbf{k})F(\mathbf{k}), \quad \text{normalized in the sense that, } \int_{\mathbb{R}^d} \boldsymbol{\xi}(\mathbf{k})d\mathbf{k} = \mathbf{0}. \tag{42}$$

Then the diffusivity and mobility coefficients are defined as

$$\mathcal{D}\ \mathrm{Id} = \int_{\mathbb{R}^d} \mathbf{v}(\mathbf{k})F(\mathbf{k})d\mathbf{k}, \text{ and } -\mu\ \mathrm{Id} = \int_{\mathbb{R}^d} \mathbf{v}(\mathbf{k})\otimes\boldsymbol{\xi}(\mathbf{k})d\mathbf{k}, \tag{43}$$

respectively, where Id denotes the identity matrix in dimension $\mathbb{R}^d$. Note that in general, we would obtain anisotropic diffusion and mobility tensor. Here due to the fact that the scattering kernel (3) is isotropic, we obtain isotropic diffusion and mobility coefficients.

Due to the normalization conditions, solutions to (41) and (42) are unique. We can then solve the two integral equations with the same numerical discretization that we just mentioned in Section 5.1. We then use (43) to obtain the diffusivity and the mobility coefficients. Later on, we will compare numerical reconstruction results based on the Boltzmann-Poisson model with those based on the drift-diffusion-Poisson model. For the comparison to make sense, the coefficients in the two models have to be calculated from the same set of material parameters. That is the main reason for us formalize the computation of those coefficients in such a way.

5.3 Regularization by parameterization

To reduce the ill-posedness of the inverse problems, we have to regularize the problem. Classical regularization strategy for numerical solution of inverse problems is to add a regularization term in the objective functional, such as in (12). Tikhonov and total variation (TV) regularization are two strategies that are mostly used in the past in inverse transport calculations [26, 27, 52]. In this work, we impose regularization by parameterize the unknowns with a small number of coefficients. We then attempt to reconstruct these coefficients. We consider mainly two type of settings.

In the first setting, we consider the reconstruction of smooth doping profiles. We use the method of Fourier coefficients. For example, in a two-dimensional rectangular domain, we decompose the unknown function into Fourier modes as

$$\mathcal{N}(\mathbf{x}) \approx \sum_{\boldsymbol{\zeta}\in\mathbb{M}} c_{\boldsymbol{\zeta}} e^{-i2\pi\boldsymbol{\zeta}\cdot\mathbf{x}}, \tag{44}$$

with $c_{-\boldsymbol{\zeta}} = \overline{c_{\boldsymbol{\zeta}}}$ to ensure that $\mathcal{N}(\mathbf{x})$ is real. Here $\boldsymbol{\zeta} = (\frac{\zeta_x}{L_x}, \frac{\zeta_y}{L_y})^t$, with $(\zeta_x,\ \zeta_y) \in \mathbb{M} = [-M_x\ M_x] \times [-M_y\ M_y]$, and L_x and L_y the size of the domain in x- and y- direction respectively. M_x and M_y are the numbers of Fourier modes to be reconstructed in x- and y-directions. To compute the gradients of the objective function with respective to $\{c_{\boldsymbol{\zeta}}\}_{\boldsymbol{\zeta}\in\mathbb{M}}$, we use the chain rule. Because the gradient with respect to $\mathcal{N}$ is already computed using the adjoint method in (25), we just need to compute the gradients of $\mathcal{N}(\mathbf{x})$ with respect to $\{c_{\boldsymbol{\zeta}}\}_{\boldsymbol{\zeta}\in\mathbb{M}}$. These gradients are given analytically by $\{\cos 2\pi\boldsymbol{\zeta}\cdot\mathbf{x}\}_{\boldsymbol{\zeta}\in\mathbb{M}}$.

In the second setting, we consider the reconstruction of discontinuous doping profiles. Here we only need to reconstruct the interface of the discontinuity (which is a co-dimension one object) and the values of the doping profile, say $\mathcal{N}^i$ and $\mathcal{N}^o$, in the regions on both sides of the interface. We regard the interface as the intersection of the domain with a closed curve Σ, centered at the origin and parameterized as $\Sigma = \{\mathbf{x} : \mathbf{x} = (r\cos\theta, r\sin\theta),\ r \text{ defined in (45)}\}$,

$$r(\theta) = \sum_{k\in\mathbb{M}} c_k e^{-i2\pi k\theta}, \tag{45}$$

where $\mathbb{M} = [-M\ M]$ and again $c_{-k} = \overline{c_k}$. The doping profile in this case can be written as

$$\mathcal{N}(\mathbf{x}) = \begin{cases} \mathcal{N}^i, & \mathbf{x} \in \Omega^I \\ \mathcal{N}^o, & \mathbf{x} \in \Omega^o \end{cases} \tag{46}$$

where Ω^I and $\Omega^o = \Omega \backslash \overline{\Omega^I}$ denote the regions of the device that are enclosed inside and outside Σ, respectively. The gradient of $\mathcal{N}$ with respect to $\{c_k\}_{k\in\mathbb{M}}$ can then be computed following the strategy in [55]. Using the fact that the outer normal direction at (r,θ) is $(\frac{dr/d\theta}{r}\sin\theta + \cos\theta, -\frac{dr/d\theta}{r}\cos\theta + \sin\theta)^{\mathfrak{T}}$, we obtain, $k \in M$,

$$\frac{d\mathcal{N}}{dc_k}(\mathbf{x}) = \begin{cases} (\mathcal{N}^i - \mathcal{N}^o)\cos 2\pi k\theta, & \mathbf{x} \in \Sigma \\ 0, & \mathbf{x} \notin \Sigma. \end{cases} \tag{47}$$

The above parameterization schemes have also been used in other inverse transport problems in slightly different settings [5]. As we have mentioned above, although Tikhonov and TV regularization can be used respectively when reconstructing smooth and discontinuous doping profiles, the parameterization schemes here provide alternatives that can reduce the size of the space where the optimal doping profiles are searched from, and thus reduce some computational cost.

5.4 Generating synthetic measurements

We will present in next section some numerical simulation with synthetic measurement data to demonstrate the performance of the reconstruction methods. By synthetic measurement data, we mean data that are generated by the Boltzmann-Poisson system (1) with the true doping profile. To avoid "inverse crimes", referring to the trivial inversion of linear systems, we generate all measurements using the forward solver with finer mesh than the mesh we used for the inverse problems. We have also generated data with a different code that is based on first order finite volume method we adapted from the discretization presented in [53]. In that finite volume discretization, we also use the Gummel iteration for the alternation between the Boltzmann equation and the Poisson equation. The mesh used in the finite volume discretization is triangular instead of the rectangular ones that are used in the discontinuous Galerkin discretization we described above. Either way, the synthetic "measurement" created this way contains discretization noise already. The noise level is roughly $1\% \sim 2\%$ according to our estimation. For the reconstructions with the drift-diffusion-Poisson model, the "measurement" data are also generated with the Boltzmann-Poisson model. In other words, we are assuming that the Boltzmann-Poisson model is the correct model for charge transport in semiconductor devices. Our conclusion on transport and diffusion comparison in Section 6 is thus based on such an assumption.

We will also present numerical results with stationary (i.e. time-independent) measured data. To generate stationary data, we run the model until the system has reach its equilibrium state. We understand that this might not be the best method to solve the stationary problem. However, it is very convenient for us since we have time-dependent code that works very well. Besides, the relaxation time from initial state to stationary state is not notoriously long in our simulation. So it is convenient for us to use the current code that we have benchmarked.

6 Numerical Examples

We now present some numerical simulations with synthetic measurement data. To reduce computational costs of the study, we consider quasi two-dimensional settings only. The domain of interest the rectangular cylinder $\Omega \times \mathbb{R} = (0,\ 2) \times (0,\ 1) \times \mathbb{R}$ with the unit of length μm. We assume the problem is invariant in z- direction so that we only need to solve the problem in the cross-section Ω. The velocity space is still three-dimensional though.

The measurements are taken on the boundary of Ω. The Dirichlet and Neumann parts of the boundary vary case by case and will be detailed below. We consider mainly three different categories of doping profile configurations: smooth functions, piecewise constant functions and specially arranged channel structures. Specific parameters used will be provided below in different cases. We emphasize here that to avoid oscillatory behavior in solutions of the BP and DDP models, we always regularize a little bit the doping profile near the jumps. The general settings for the geometry and the doping profiles are depicted in Fig. 1 where

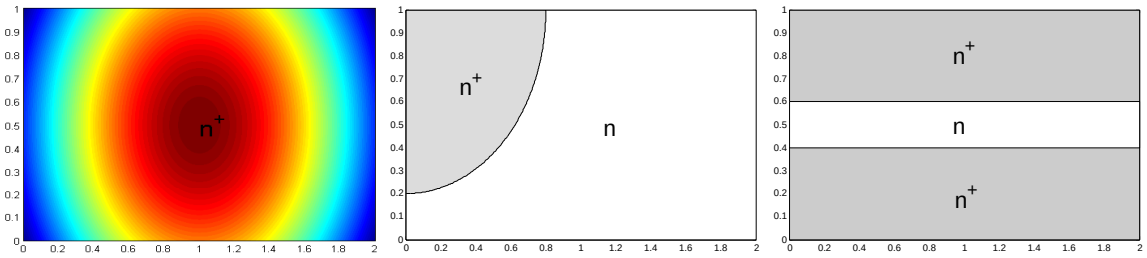

Figure 1: Domain and typical doping profiles in the numerical simulations. From left to right are continuous doping profile, piecewise constant doping profile and the doping profile that forms a $n^+ - n - n^+$ channel.

n^+ denotes the regions that are highly doped. The unit of the doping density is 10^{16} cm^{-1} in all of the following simulations. There are a total number of $N_S = 20$ boundary applied potentials used. For practical reasons, we limited the applied potential φ_D on each part of the boundary to be multiples of hat functions centered at the middle of the part of the boundary. The multiplication constant is in the range $[0.5\ 2.0]$ V. The reconstruction, unless specified, are done with time-dependent data in the time interval $(0,\ 6)$ picoseconds.

6.1 Recovering smooth doping profiles

We start with the reconstructions of smooth doping profiles. By smooth, we simply mean regular enough. Even though smooth doping profile is of less interest in many literature on semiconductor modeling, reconstruction of those profiles can indeed help us to test the validity of the reconstruction algorithms. The reconstructions are done by parameterizing the unknown profile by Fourier coefficients as in (44) and only reconstructing the first 15×15 Fourier modes ($M_x = M_y = 15$ in (44)). We performed reconstructions on two profiles. They are, respectively,

$$\mathcal{N}^1(\mathbf{x}) = 10 + 3\exp(-\frac{(\frac{x}{L_x} - 1)^2 + (\frac{y}{L_y} - 0.5)^2}{0.05}) \quad \text{and} \quad \mathcal{N}^2(\mathbf{x}) = 10 + 2\sin(\frac{2\pi(x + 0.15L_x)}{L_x}). \tag{48}$$

where $L_x = 2$ and $L_y = 1$. The maximum value of $\mathcal{N}^1$ is $\mathcal{N}^1_{\max} = 13$ units and the minimum value is $\mathcal{N}^1_{\min} \approx 10$ units. The maximum value of $\mathcal{N}^2$ is $\mathcal{N}^2_{\max} = 12$ units and the minimum value is $\mathcal{N}^2_{\min} = 8$ units. The shifting factor $0.15L_x$ is intentionally presented to make sure that the doping profile has more than a single non-zero Fourier modes in the domain.

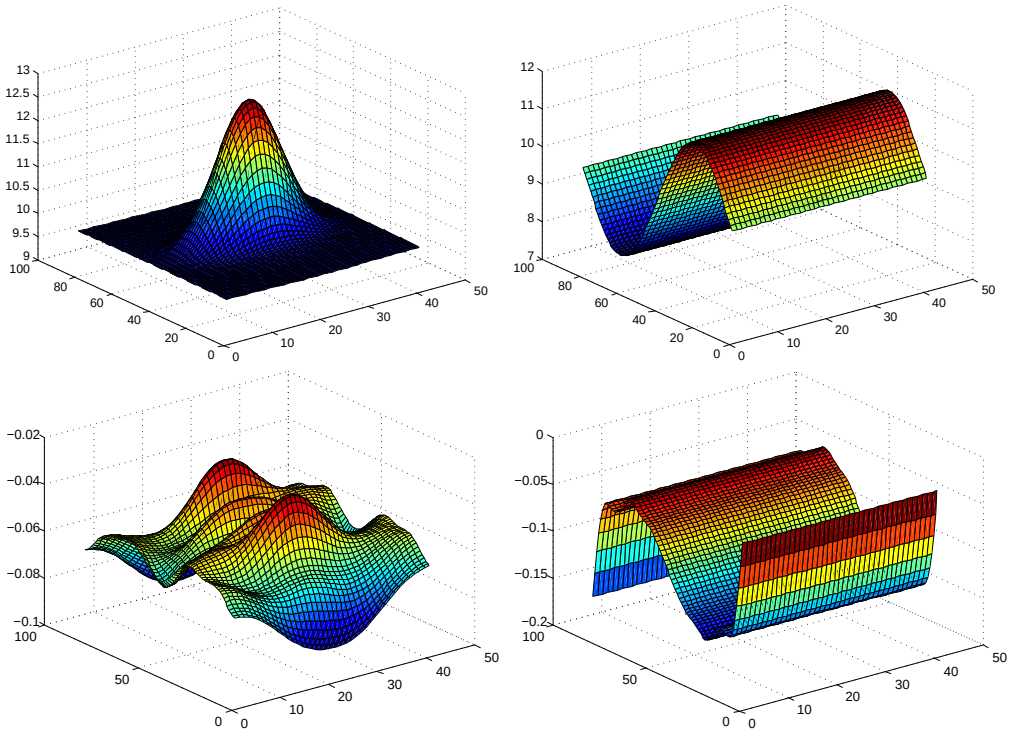

Figure 2: The reconstructions of the two continuous doping profiles $\mathcal{N}^1$ and $\mathcal{N}^2(\mathbf{x})$ with full boundary measurements. Top row: reconstructed profiles with noise-free data; Bottom row: difference between reconstructed profiles and true profiles.

We show in Fig. 2 and Fig. 3 the reconstruction results with measurements collected on the whole boundary of the domain. We observe that in this setting, the reconstructions are very accurate when the data used contain no random noise; see Fig. 2. The relative L^2 error, defined as L^2 norm of the difference between true profile and reconstructed profile over L^2 norm of the true doping profile, in the reconstructions are 2.2% for $\mathcal{N}^1$ and 2.4% for $\mathcal{N}^2$. When the data used contain a moderate amount of noise, the reconstructions of the low Fourier modes are still relatively accurate but higher Fourier modes start to deviate; see Fig. 3. The relative error in the reconstructions are 5.8% for $\mathcal{N}^1$ and 5.7% for $\mathcal{N}^2$ respectively.

To study the reconstruction with less data, we repeat the simulations in Fig. 2 with measurements taken only on the top and bottom parts of the boundary. The results are presented in Fig. 4. The quality of the reconstructions are not as high as the previous cases with full boundary measurements. However, the reconstructions are still reasonably accurate, with relative errors 5.6% for $\mathcal{N}^1$ and 7.8% for $\mathcal{N}^2$ when noise-free data are used. When noisy data with 5% noise is used, the quality of the reconstructions degenerate significantly. Typical relative errors that are around 11%∼13%. However, in special cases when the real-

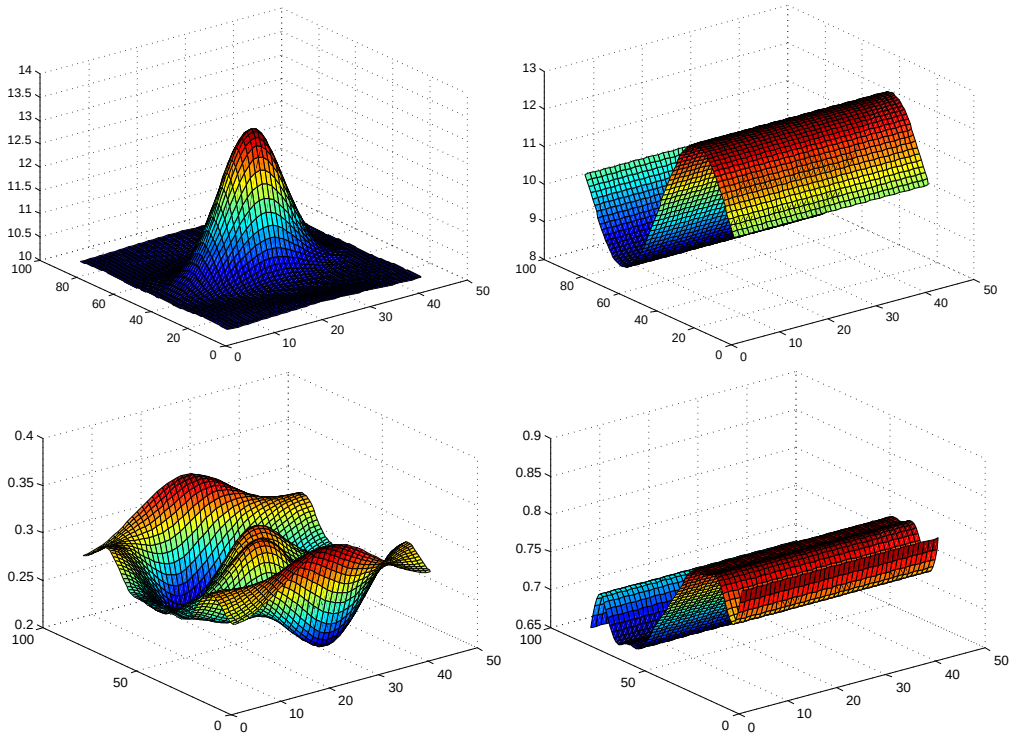

Figure 3: Same as Fig. 2 except that the reconstructions are done with a typical realization of noisy data containing 5% random noise.

ization of the noise is very non-typical, the relative errors in the reconstruction can be very large. For example, in the reconstructions presented in Fig. 5, the relative errors are 18.7% for $\mathcal{N}^1$ and 21.3% for $\mathcal{N}^2$ respectively.

6.2 Recovering discontinuous doping profiles

We now investigate the reconstruction of discontinuous doping profiles with full and partial boundary measurements. We emphasize here again that, to avoid highly oscillatory solutions of the Boltzmann-Poisson system, we regularize the doping profiles across the discontinuities to make the transition smooth. The regularization is weak so that the gradient of the doping profiles is still very large in the transition region that overall the doping function looks like a piecewise continuous function.

In the first numerical test here, we assume that the values of the doping profile is known on both sides of the discontinuity. We thus only need to reconstruct the interface of the discontinuity. We present in Fig. 6 two typical reconstructions with measurements on the whole boundary. The relative errors, in this case computed as the relative L^2 norm of the curve that form the interface, are 1.6% and 1.8% respectively with noise-free data while 2.7% and 2.9% respectively with noisy data contain 5% random noise. The same numerical test is then repeated with measured data only on the top and bottom boundaries. The result is presented in Fig. 7. We observe by comparing results in Fig. 6 and Fig. 7 that the reconstruction is very stable when the measurement is everywhere on the boundary.

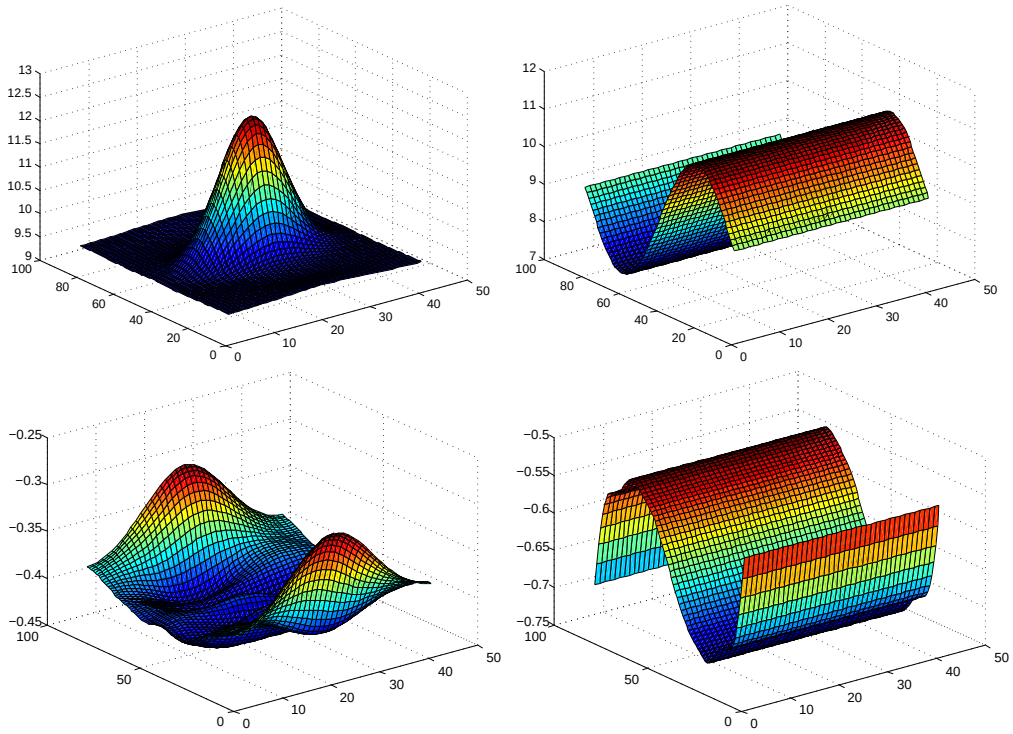

Figure 4: The reconstructions of the two continuous doping profiles $\mathcal{N}^1$ and $\mathcal{N}^2$ with measurements only on the top and bottom parts of the boundary. Top row: reconstructed profiles with noise-free data; Bottom row: difference between reconstructed profiles and true profiles.

Otherwise, the reconstruction is very sensitive to the noise in data; as we can see from the plots in Fig. 7. Keep in mind that this result is obtained in the case where only the interface of discontinuity is to be reconstructed.

Two more numerical simulations are presented in Fig. 8 where both the interface of discontinuity and the values of the doping profile on both sides of the interface reconstructed simultaneously. The reconstructions of the boundaries look very similar to those in Fig. 7, with quality that is a little bit lower. The values of the constant profiles are reconstructed relatively accurately in the two cases also. The true doping values for the n^+ and n regions are $(\mathcal{N}^{1,i},\ \mathcal{N}^{1,o}) = (11.0,\ 9.0)$ for both cases in Fig. 8 and the reconstructed values (when noise-free data are used) are $(\mathcal{N}^{1,i},\ \mathcal{N}^{1,o}) = (10.8,\ 9.1)$ and $(\mathcal{N}^{1,i},\ \mathcal{N}^{1,o}) = (10.9,\ 9.2)$ respectively for the two configurations. Note that the reconstructed total doping, the product of the area of the region multiplied by the value inside the region is recovered almost exactly. This indicates that the reconstruction process preserve the first moment of the profile, which is important in practice.

The above numerical experiments show that the reconstruction of discontinuous doping profile can be achieved with reasonable accuracy if we parameterize the unknown appropriately as in Section 5.3 and measure the data with little noise. When full measurements are available, our numerical experience shows that we can reconstruct the profile very stably.

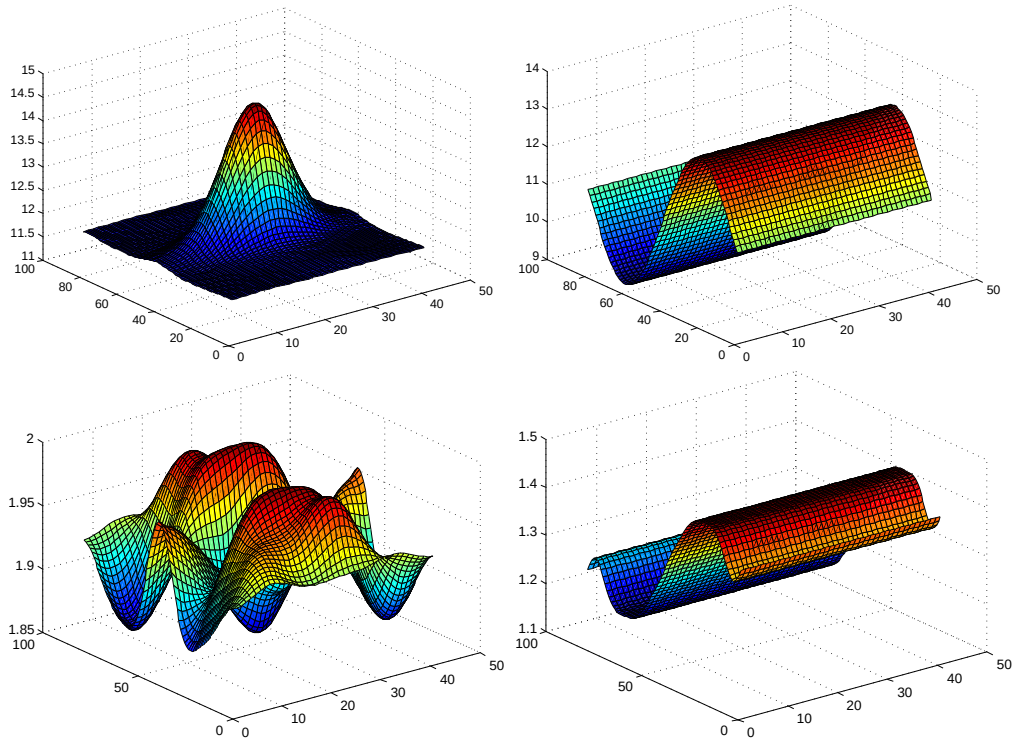

Figure 5: Same as Fig. 4 except that the reconstructions are done with a realization of noisy data containing 5% random noise. The noise presented in the data set is chosen specially with non-zero mean.

6.3 Drift-diffusion versus Boltzmann

We have seen that the reconstructions based on the Boltzmann-Poisson model are relatively accurate in many cases. We now compare reconstructions based on the BP model and the reconstructions based on DDP model. The idea is to view the BP model as the "right" model for electron transport in semiconductor device and treat the DDP model as an approximation to it (and thus less accurate). There have been numerical simulations showing that the two models can generate results that are significantly different. However, it is not clear so far how this difference will have effect on the reconstruction results. This motivates the comparison. The measurements used in the following simulations are all generated using the Boltzmann-Poisson system.

We present two sets of comparisons in Fig. 9: the reconstructions with full boundary measurements and the reconstructions with partial boundary measurements. It is clear from the top-left plot of Fig. 9 that there are significant difference between the reconstructions and the BP-based reconstruction is closer to the true interface. The difference disappear when we the noise in the measurement is high enough; see the top-right plot in Fig. 9. Similar results are observed when we have only partial measurements, though in this case the difference between the reconstructions are smaller even when noise-free data are used.

It is well-known that when the doping is strong in a small region of the device and the applied potential is very strong, the DDP model fails significantly to approximate the transport phenomenon. To see how this fact is reflected on the reconstructions, we now

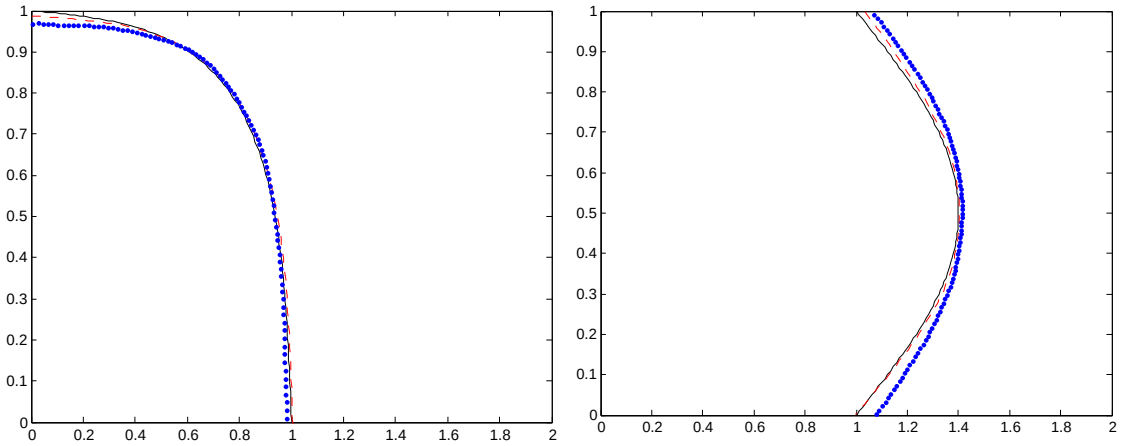

Figure 6: Two typical reconstructions of jump interfaces of piecewise constant doping profiles with measurements on the whole boundary. Plotted are real jump interface (black solid), reconstruction with noise-free data (red dashed) and reconstruction with data containing 5% random noise (blue dotted).

compare the reconstructions in this setting. As before, we avoid oscillation of the solutions to the DDP and BP models, we regularize the doping profile slightly to get a smooth transition. The reconstructions are shown in Fig. 10. In all the reconstructions, we assume the profile is translational invariant along x-direction so that we need only to reconstruct the distribution in y-direction. Thus the data measured along x-direction is averaged to get the data for the one-dimensional problem. Same as in Section 5.3, we parameterize the profile with Fourier modes (since the profile is regularized), so that we need only to reconstruct a few Fourier coefficients. The profiles are then constructed by summation of all reconstructed Fourier modes.

6.4 Reconstructions with stationary data

In the last set of numerical experiments, we present some reconstructions with stationary data based on the Boltzmann-Poisson model. Stationary data have been used in most of the previous studies on the subject of recovering doping profiles. It is well-known that stationary data contains much less information than time-dependent data. So we can expect that the reconstructions with stationary data is less accurate than those with time-dependent data that we just presented.

We first consider the reconstruction of the two doping profiles in (48) with noise-free stationary data. We show the reconstructions with data on the whole boundary of the domain in Fig. 11. The relative errors in the two reconstructions are 9.7% and 8.9%, respectively, larger than those in the results of Fig. 2. We observe from our numerical experiments that when noise data are used, or when data only on part of the boundary are used, the difference between time-dependent and stationary reconstructions is even larger. This concludes that stationary data indeed give less accurate reconstructions when we attempt to reconstruct continuous doping profiles.

We observe also slightly less accurate reconstructions when we recover discontinuous

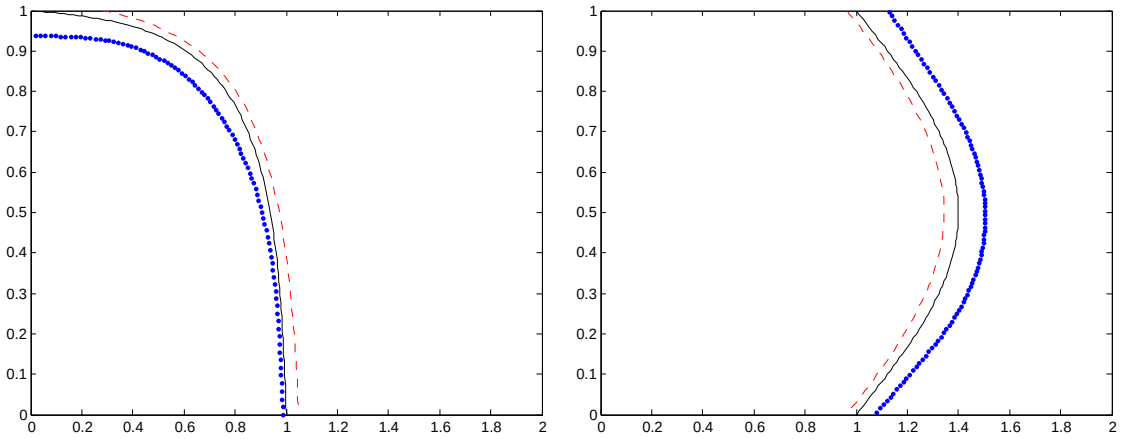

Figure 7: Same as in Fig. 6 except that the reconstructions are now performed with measured data only on the top and bottom parts of the boundary.

doping profiles. In Fig. 12, we present the several reconstructions of interfaces of discontinuity with stationary data. We see that in both the case when data are measured on the whole boundary and the case when data are measured only on the top and bottom parts of the boundary, the reconstructions are not as accurate as those done with stationary data as presented in the previous sections. More specifically, the relative errors computed in the left plots of Fig. 12 are 6.7% (noise-free data) and 7.9% (noisy data) when measurements on the whole boundary are available and 7.4% (noise-free data) and 8.8% (noisy data) when only measurements on the top and bottom boundary are available. The numbers for the right plots in Fig. 12 are very similar.

7 Conclusions and Remarks

We studied an inverse problem related to the Boltzmann-Poisson system of equations for transport of electrons in semiconductor devices. We presented linear reconstructions algorithms as well as nonlinear algorithms of Newton type to recover numerically the doping profile function from measurements of device characteristics, that is the voltage-to-current map. To reduce the degree of ill-posedness of the inverse problem, we proposed to parameterize the unknown doping profile function to reduce the number of unknowns in the inverse problem. We showed by numerical examples that the reconstruction of a few low moments of the doping profile is possible when accurate measurements are available. We have discussed the reconstruction of both piecewise constant and more smooth doping profiles.

We have compared the reconstruction with the reconstructions based on the drift-diffusion model. In the settings that we are interested, the two reconstructions are sufficiently different. However, as the size of the device getting larger and larger, or the noise level in the data getting higher and higher, the differences in the reconstructions are indistinguishable. The reconstruction with the transport model is significantly slower than reconstructions with the drift-diffusion-Poisson model. In general, hundreds of forward and adjoint models need to be solved before the reconstruction algorithms converge.

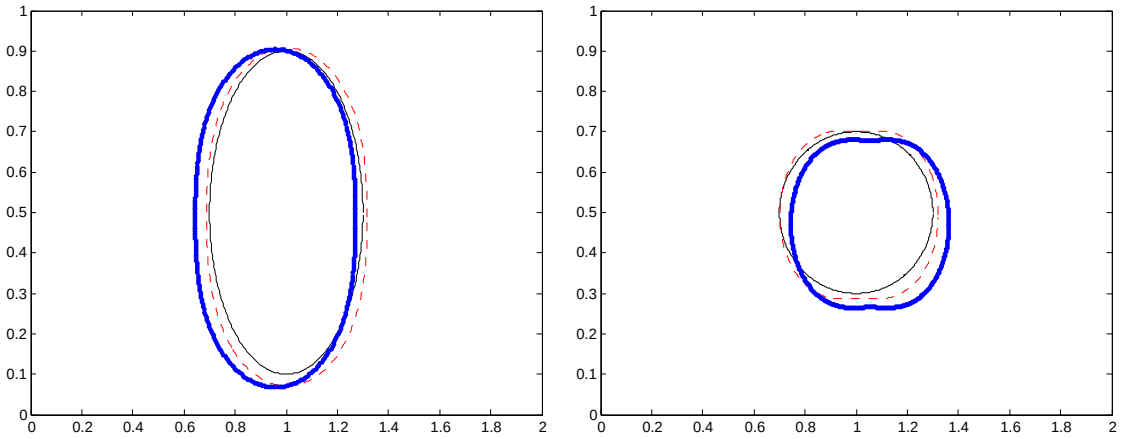

Figure 8: Reconstructions of jump interfaces of piecewise constant doping profiles with measurements on the top and bottom boundary. Plotted are real jump interface (black solid), reconstruction with noise-free data (red dashed) and reconstruction with data containing 5% random noise (blue dotted).

One may argue that the reconstructions based the drift-diffusion-Poisson equation can be improved if we also look for the best diffusion and mobility coefficients that match the measured data. We intentionally avoid such a scenario because the reconstruction problem become overwhelmingly complicated in that scenario. It is highly possible that the problem of reconstructing $\mathcal{D}(\mathbf{x})$, $\mu(\mathbf{x})$ and $\mathcal{N}(\mathbf{x})$ simultaneously has no unique solution at all even with full time-dependent boundary measurements. Even if there is uniqueness, the reconstruction must be extremely unstable as we have seen from this paper that the reconstruction of one unknown $\mathcal{N}(\mathbf{x})$ is already very ill-posed. We acknowledge, however, that the diffusivity and mobility parameters can indeed be fitted from experimental data under much simplified setting; see for example the discussion in [10, 51, 56].

To deal with the ill-posedness of the inverse problem, we parameterized the doping profile to reduce the number of unknowns to be reconstructed. The number of modes kept in the parameterization, say M, can be viewed as the regularization parameter. When $1/M$ is large, we have a small number of unknown to be reconstructed. The problem is strongly regularized in this case. On the other hand, when $1/M$ is small, the problem is less strongly regularized. The classical regularization strategy, such as the Tikhonov and the total variation regularizations can also be adopted in our computation. Detail comparison between various regularization strategies in the settings of smooth and discontinuous doping profiles are currently under investigation.

The mismatch term in the objective functional (12) can be replaced by the L^1 norm of the difference between model prediction and measurement. The resulted minimization problem, however, has to be solved using methods that are different from what is presented in this paper. Also, the norm used in the mismatch term and the one used in the regularization term need not be the same. For example, one can minimize (12) with L^1 in the first term and L^2 (Tikhonov) in the regularization term as we was proposed in [26, 27]. How would the combinations of different norms affect the results of the doping reconstruction is a topic deserves further investigation.

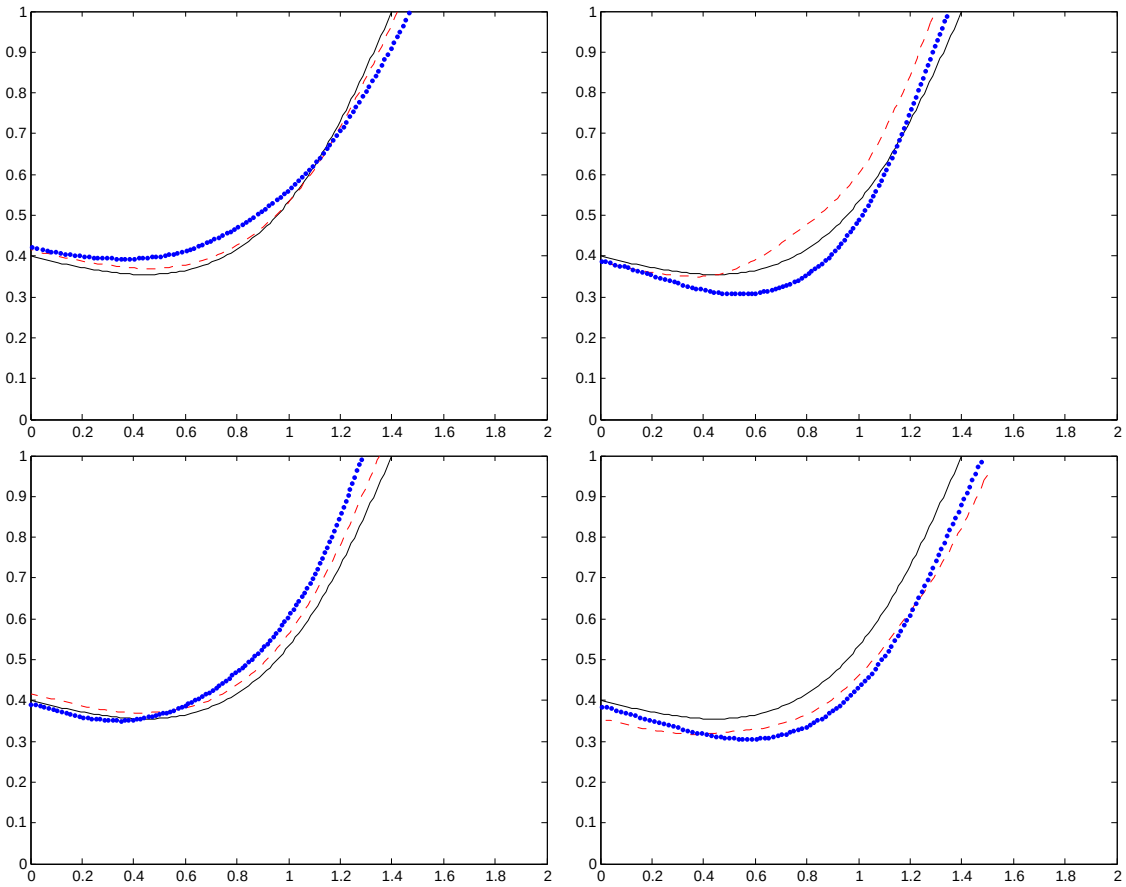

Figure 9: Comparison of reconstructions with Boltzmann-Poisson model (red dashed) and those with drift-diffusion-Poisson model (blue dotted) with the true profiles (black solid). Top row: measurements on whole boundary; Bottom row: measurement only on top and bottom parts of the boundary. Left: noise-free data; Right: data with 5% noise.

The Boltzmann-Poisson model we employed in this study is a simplified version of the full Boltzmann-Poisson system for semiconductor device that include another Boltzmann equation for transport of holes. Furthermore, the two Boltzmann equations are coupled through recombination and generation of electron-hole pairs. Further study with full model will be discussed in the future. Although the full system is more complicated than the current system we are using, the numerical techniques we have here can still be applied in a straightforward way. Whether or not we can observe similar phenomenon for this full model is something under investigation. Reconstructions with more complicated macroscopic models, such as the high-field drift-diffusion-Poisson model [15, 50] can also be considered.

Let us remark finally that the numerical minimization scheme that we adopted in this study can be slightly modified to study a closely related problem for the Boltzmann-Poisson system: optimal design of doping profiles. The objective in this problem is to design doping profiles that can produce certain desired device characteristics; see [9, 21] and references there. Optimal design problems are usually posed as very similar numerical minimization problems as what we have in this paper. We are currently attempt to apply the numerical

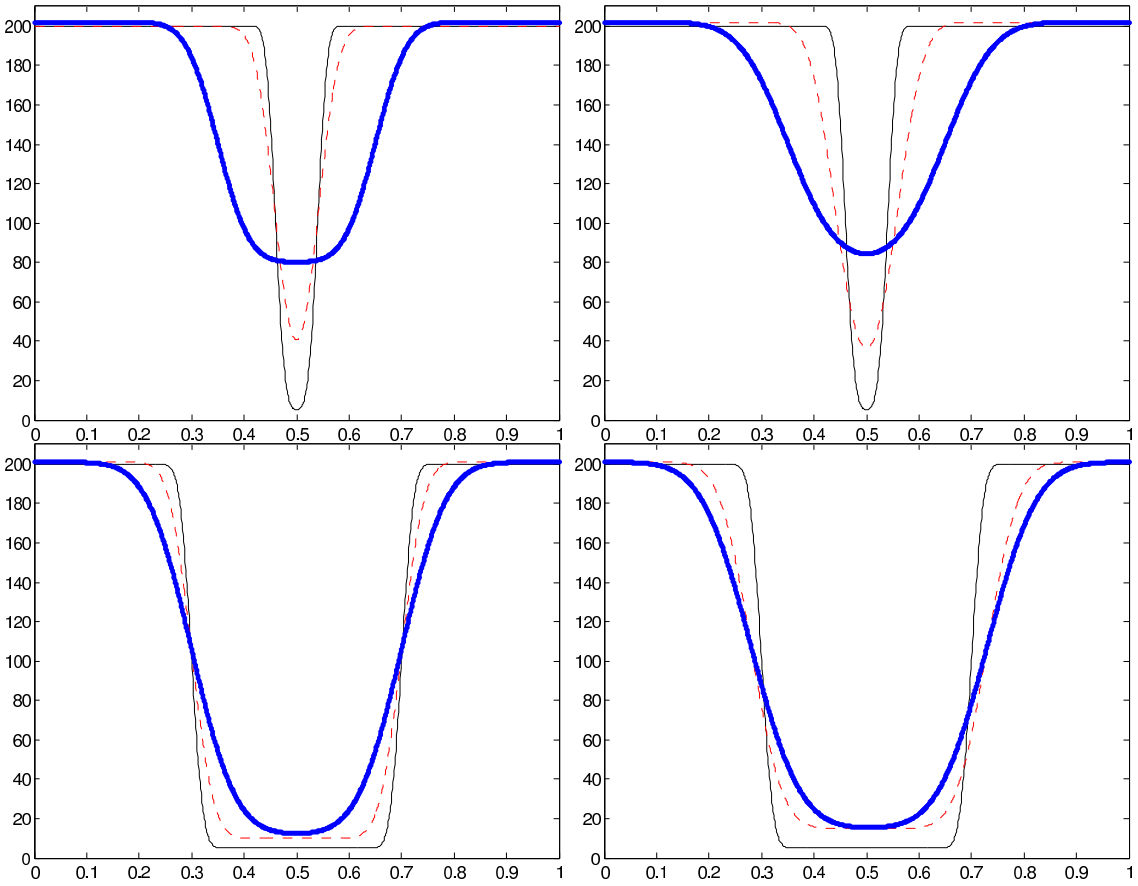

Figure 10: Reconstruction of two doping profiles that display channel effect. Top: the channel is 0.08 unit in width; Bottom: the channel is 0.4 unit in width; Left: reconstructions with noise-free data. Right: Reconstructions with noisy data of 5% noise.

methods we have to investigate the optimal design problem (also a nonlinear minimization problem).

Acknowledgment

The work of YC and IMG are supported by the National Science Foundation grant DMS-0807712 and DMS-0757450. The work of KR is supported by NSF grant DMS-0914825 and a startup grant from the University of Texas at Austin. KR also acknowledges fruitful discussions with Professor Guillaume Bal (Columbia University) regarding this work.

References

[1] N. B. Abdallah and M. L. Tayeb, *Diffusion approximation for the one dimensional Boltzmann-Poisson system*, Discrete Contin. Dyn. Syst. Ser. B, 4 (2004), pp. 1129–1142.

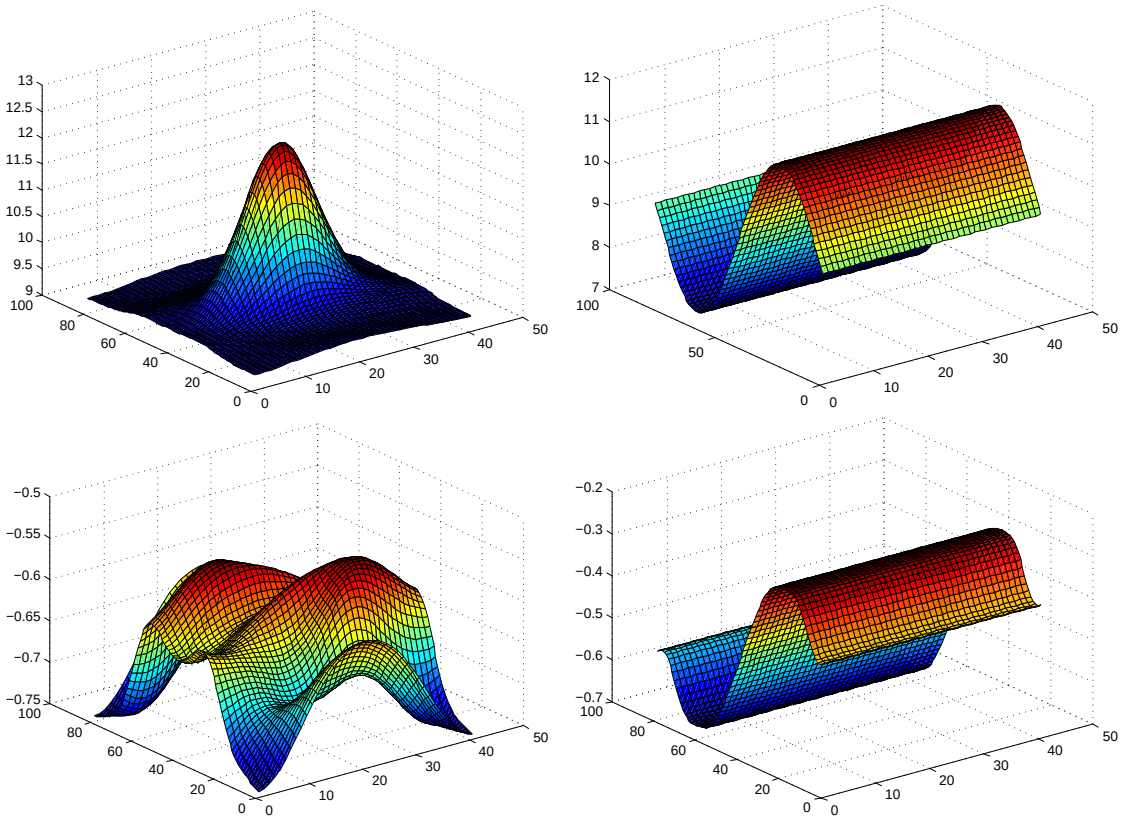

Figure 11: Reconstructions of two continuous doping profiles with noise-free stationary data. Top row: the reconstructions; Bottom row: the differences between reconstructed and true profiles.

[2] G. S. Abdoulaev, K. Ren, and A. H. Hielscher, *Optical tomography as a PDE-constrained optimization problem*, Inverse Probl., 21 (2005), pp. 1507–1530.

[3] G. Ali, I. Torciollo, and S. Vessella, *Inverse doping problems for a P-N junction*, Journal of Inverse and Ill-posed Problems, 14 (2006), pp. 537–546.

[4] A. M. Anile, W. Allegretto, and C. Ringhofer, *Mathematical Problems in Semiconductor Physics*, Lecture Notes in Mathematics, Springer-Verlag, Berlin, 2003.

[5] S. R. Arridge, O. Dorn, J. P. Kaipio, V. Kolehmainen, M. Schweiger, T. Tarvainen, M. Vauhkonen, and A. Zacharopoulos, *Reconstruction of subdomain boundaries of piecewise constant coefficients of the radiative transfer equation from optical tomography data*, Inverse Problems, 22 (2006), pp. 2175–2196.

[6] G. Bal, *Inverse transport theory and applications*, Inverse Problems, 25 (2009). 053001.

[7] N. Ben Abdallah and P. Degond, *On a hierarchy of macroscopic models for semiconductors*, J. Math. Phys., 37 (1996), pp. 3306–3333.

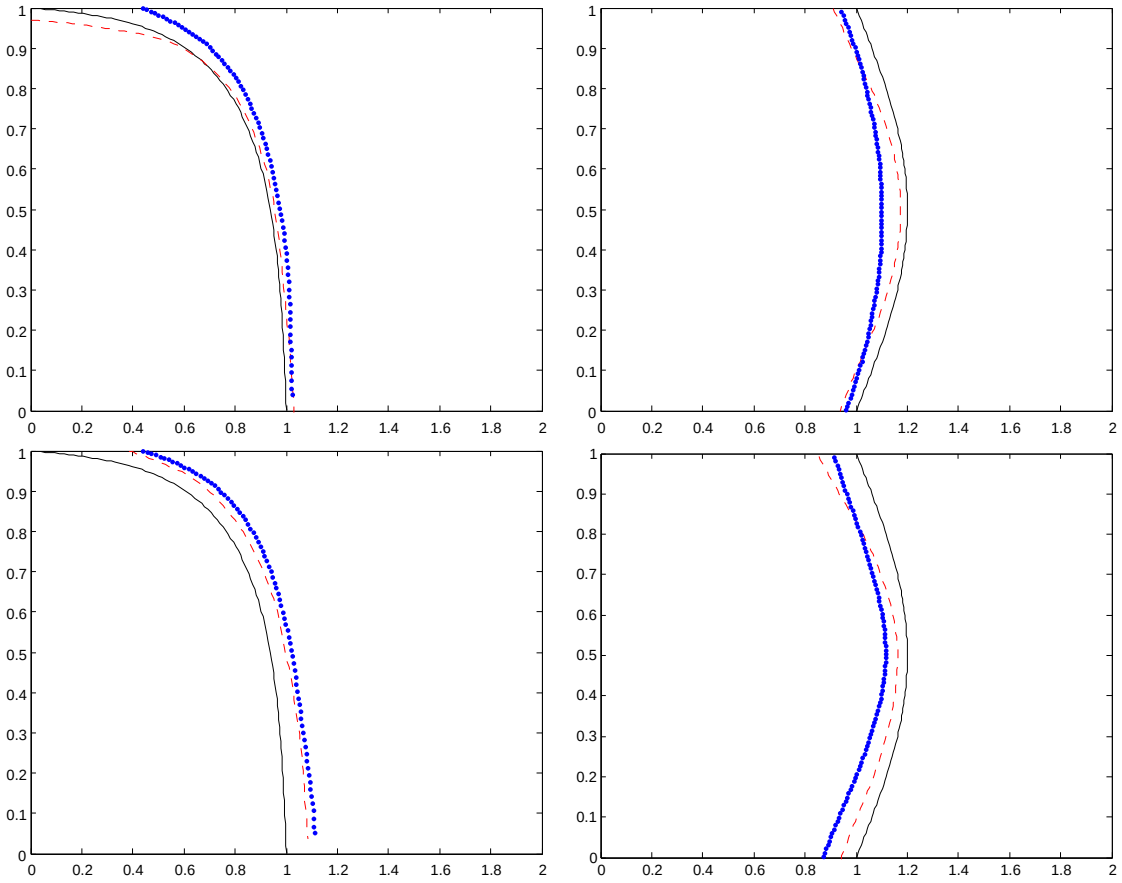

Figure 12: Typical reconstructions of discontinuous doping profiles with stationary data. Top row: data measured on full boundary; Bottom row: data measured on top and bottom part of the boundary. Plotted are true profiles (black solid), reconstructions with noise-free data (red dashed) and reconstructions with data contain 5% random noise (blue dotted).

[8] M. Burger, H. W. Engl, and P. A. Markowich, *Inverse doping problems for semiconductor devices*, in Recent Progress in Computational and Applied PDEs, Kluwer, Kluwer Academic, 2002, pp. 39–54.

[9] M. Burger and R. Pinnau, *Fast optimal design of semiconductor devices*, SIAM J. Appl. Math, 64 (2003), pp. 108–126.

[10] C. Canali, F. Nava, and L. Reggiani, *Drift velocity and diffusio coefficients from time-of-flight measurements*, in Hot-Electron Transport in Semiconductors, L. Reggiani, ed., Springer-Verlag, Berlin, 1985.

[11] J. A. Carrillo, I. Gamba, and C.-W. Shu, *Computational macroscopic approximations to the one-dimensional relaxation-time kinetic system for semiconductors*, Physica D, 146 (2000), pp. 289–306.

[12] J. A. Carrillo, I. M. Gamba, A. Majorana, and C.-W. Shu, *A direct solver for 2d non-stationary Boltzmann-Poisson systems for semiconductor devices: a MESFET simulation by WENO-Boltzmann schemes*, J. Comput. Electron., 2 (2003), pp. 375–380.

[13] ——, *A WENO-solver for the transients of Boltzmann-Poisson system for semiconductor devices: performance and comparisons with Monte Carlo methods*, J. Comput. Phys., 184 (2003), pp. 498–525.

[14] J. A. Carrillo, I. M. Gamba, A. Majorana, and C.-W. Shu, *2d semiconductor device simulations by WENO-Boltzmann schemes: efficiency, boundary conditions and comparison to Monte Carlo methods*, J. Comput. Phys., 214 (2006), pp. 55–80.

[15] C. Cercignani, I. M. Gamba, and C. D. Levermore, *A drift-collision balance asymptotic for a Boltzmann-Poisson system in bounded domains*, SIAM J. Appl. Math., 61 (2001), pp. 1932–1958.

[16] S. Chen, W. E, Y. Liu, and C.-W. Shu, *A discontinuous Galerkin implementation of a domain decomposition method for kinetic-hydrodynamic coupling multiscale problems in gas dynamics and device simulations*, J. Comput. Phys., 225 (2007), pp. 1314–1330.

[17] Y. Cheng, I. M. Gamba, A. Majorana, and C.-W. Shu, *Discontinuous Galerkin solver for Boltzmann-Poisson transients*, J. Comput. Electron., 7 (2008), pp. 119–123.

[18] ——, *A discontinuous Galerkin solver for Boltzmann-Poisson systems in nano devices*, Comput. Methods Appl. Mech. Engrg., 198 (2009), pp. 3130–3150.

[19] C. Y.-T. Chiang, C. T. Hsu, Y. T. Yeow, and R. Ghodsi, *Measurement of MOSFET substrate dopant profile via inversion layer-to-substrate capacitance*, IEEE Trans. Electron Dev., 40 (1998), pp. 1732–1736.

[20] P. Degond, T. Goudon, and F. Poupaud, *Diffusion limit for non homogeneous and non-micro-reversible processes*, Indiana Univ. Math. J, 49 (2000), pp. 1175–1198.

[21] C. R. Drago and R. Pinnau, *Optimal dopant profiling based on energy-transport semiconductor models*, Math. Models Meth. Appl. Sci., 18 (2008), pp. 195–241.

[22] W. Fang and K. Ito, *Reconstruction of semiconductor doping profile from laser-beam-induced current image*, SIAM J. Appl. Math., 54 (1994), pp. 1067–1082.

[23] ——, *Identification of contact regions in semiconductor transistors by level-set methods*, J. Comput. Appl. Math., 159 (2003), pp. 399–410.

[24] X. H. Fu and J. N. Chen, *A point-by-point multiple-sweep numerical algorithm for dopant profiling based on C-V data*, Solid-State Electronics, 35 (1992), pp. 181–185.

[25] M. Galler, *Multigroup equations for the description of the particle transport in semiconductors*, World Scientific, 2005.

[26] H. Gao and H. Zhao, *Multilevel bioluminescence tomography based on radiative transfer equation. part 1: l1 regularization*, Optics Express, 18 (2010), pp. 1854–1871.

[27] ——, *Multilevel bioluminescence tomography based on radiative transfer equation. part 2: total variation and l1 data fidelity*, Optics Express, 18 (2010), pp. 2894–2912.

[28] D. A. Gore and D. A. Drew, *The one-dimensional inverse doping problem in semiconductor device modeling*, Inverse Problems in Science and Engineering, 1 (1994), pp. 27–43.

[29] Y. He and D. E. Keyes, *Reconstructing parameter of the FitzHugh-Nagumo system from boundary potential measurements*, J. Comput. Neurosci., 22 (2007), pp. 251–264.

[30] S. Holzer, R. Minixhofer, C. Heitzinger, J. Fellner, T. Grasser, and S. Selberherr, *Extraction of material parameters based on inverse modeling of three-dimensional interconnect fusing structures*, Microelectronics Journal, 35 (2004), pp. 805–810.

[31] S. Holzer and S. Selberherr, *Optimization issue in interconnect analysis*, in Proceedings of the 25th International Conference on Microelectronics, 2006, pp. 465–470.

[32] C. Jacoboni and P. Lugli, *The Monte Carlo Method for Semiconductor Device Simulation*, Springer-Verlag, Wien, 1989.

[33] J. W. Jerome, *Analysis of Charge Transport: A Mathematical Study of Semiconductor Devices*, Springer-Verlag, Berlin, 1996.

[34] W. C. Johnson and P. T. Panousis, *The influence of Debye length on the C-V measurement of doping profiles*, IEEE Trans. Electron Devices, ED-18 (1971), pp. 965–973.

[35] A. Jüngel, *Transport Equations for Semiconductors*, Springer, Berlin, 2009.

[36] D. P. Kennedy, P. C. Murley, and W. Kleinfelder, *On the measurement of impurity atom distributions in silicon by the differential capacitance technique*, IBM J. Res. Develop., 12 (1968), pp. 399–409.

[37] ——, *On the measurement of impurity atom distributions in silicon by the differential capacitance technique*, IBM J. Res. Develop., 13 (1969), pp. 212–214.

[38] A. D. Kim, C. Hayakawa, and V. Venugopalan, *Estimating tissue optical properties using the Born approximation of the transport equation*, Optics Lett., 31 (2006), pp. 1088–1090.

[39] A. D. Klose, V. Ntziachristos, and A. H. Hielscher, *The inverse source problem based on the radiative transfer equation in optical molecular imaging*, J. Comput. Phys., 202 (2005), pp. 323–345.

[40] H. Kroemer and W. Chien, *On the theory of Debye averaging in the C-V profiling of semiconductors*, Solid-State Electronics, 24 (1981), pp. 655–660.

[41] A. Leitão, P. A. Markowich, and J. P. Zubelli, *On inverse doping profile problems for the stationary voltage-current map*, Inverse Probl., 22 (2006), pp. 1071–1088.

[42] Y. Li and C.-K. Chen, *A simulation-based evolutionary technique for inverse doping profile problem of sub-65 nm CMOS devices*, J. Comput. Electron., 5 (2006), pp. 365–370.

[43] A. Majorana and R. Pidatella, *A finite difference scheme solving the Boltzmann-Poisson system for semiconductor devices*, J. Comput. Phys., 174 (2001), pp. 649–668.

[44] P. A. Markowich, C. A. Ringhofer, and C. Schmeiser, *Semiconductor Equations*, Springer, New York, 1990.

[45] N. Masmoudi and M. L. Tayeb, *On the diffusion limit of a semiconductor Boltzmann-Poisson system without micro-reversible process*, Commun. Part. Diff. Eqns., 35 (2010), pp. 1163–1175.

[46] R. A. Moline, *Ion implanted phosphorus in silicon: profiles using C-V analysis*, J. Appl. Phys., 42 (1971), pp. 3553–3558.

[47] G. J. L. Ouwerling, *Physical parameter extraction by inverse device modelling: Application to one- and two-dimensional doping profiling*, Solid-State Electronics, 33 (1990), pp. 757–771.

[48] ——, *A problem-specific inverse method for two-dimensional doping profile determination from capacitance-voltage measurements*, Solid-State Electronics, 34 (1991), pp. 197–214.

[49] F. Poupaud, *On a system of nonlinear Boltzmann equations of semiconductor physics*, SIAM J. Appl. Math, 50 (1990), pp. 1593–1606.

[50] ——, *Runaway phenomena and fluid approximation under high fields in semiconductor kinetic theory*, Z. Angew. Math. Mech., 72 (1992), pp. 359–372.

[51] Y. K. Pozhela, *Transport parameters from microwave conductivity and noise measurement*, in Hot-Electron Transport in Semiconductors, L. Reggiani, ed., Springer-Verlag, Berlin, 1985.

[52] K. Ren, *Recent developments in numerical techniques for transport-based medical imaging methods*, Commun. Comput. Phys., 8 (2010), pp. 1–50.

[53] K. Ren, G. Bal, and A. H. Hielscher, *Frequency domain optical tomography based on the equation of radiative transfer*, SIAM J. Sci. Comput., 28 (2006), pp. 1463–1489.

[54] C. Ringhofer, C. Schmeiser, and A. Zwirchmayr, *Moment methods for the semiconductor Boltzmann equation on bounded position domains*, SIAM J. Numer. Anal., 39 (2001), pp. 1078–1429.

[55] F. Santosa, *A level-set approach for inverse problems involving obstacles*, ESAIM: Control, Optimization and Calculus of Variations, 1 (1996), pp. 17–33.

[56] A. Schenk, *Advanced Physical Models for Silicon Device Simulation*, Springer-Verlag, Wien, 1998.

[57] C. Schmeiser and A. Zwirchmayr, *Elastic and drift-diffusion limits of electron-phonon interaction in semiconductors*, Math. Models Methods Appl. Sci., 8 (1998), pp. 37–53.

[58] D. K. Schroder, *Semiconductor Material and Device Characterization*, John Wiley & Sons, Hoboken, New Jersey, 3rd ed., 2006.

[59] D. Schroeder, *Modelling of Interface Carrier Transport for Device Simulation*, Springer-Verlag, Wien, 1994.

[60] S. Selberherr, *Analysis and Simulation of Semiconductor Devices*, Springer-Verlag, Vienna, Austria, 1984.

[61] V. I. Shashkin, I. R. Karetnikova, and A. Murel, *Approach to electrochemical C-V profiling in semiconductor with sub-Debye-length resolution*, IEEE Trans. Electron Devices, 47 (2000), pp. 1221–1224.

[62] C. R. Vogel, *Non-convergence of the L-curve regularization parameter selection method*, Inverse Probl., 12 (1996), pp. 535–547.

[63] ——, *Computational Methods for Inverse Problems*, Frontiers in Applied Mathematics, SIAM, Philadelphia, 2002.

[64] S. J. Wang, J. Y. Lee, and C. Y. Chang, *An efficient and reliable approach for semiconductor device parameter extraction*, IEEE Trans. Computer-Aided Design, 5 (1986), pp. 170–178.

[65] D. E. Ward and K. Doganis, *Optimized extraction of MOS model parameters*, IEEE Trans. Computer-Aided Design, 1 (1982), pp. 163–168.

[66] C. C. Williams, *Two-dimensional dopant profiling by scanning capacitance microscopy*, Annu. Rev. Mater. Sci., 29 (1999), pp. 471–504.

[67] M.-T. Wolfram, *Inverse dopant profiling from transient measurements*, J. Comput. Electron., 6 (2007), pp. 409–420.

[68] P. Yang and P. K. Chatterjee, *An optimal parameter extraction program for MOSFET models*, IEEE Trans. Electron Devices, 30 (1983), pp. 1214–1219.

[69] L. Zeni, R. Bernini, and R. Pierri, *Reconstruction of doping profiles in semiconductor materials using optical tomography*, Solid-State Electronics, 43 (1999), pp. 761–769.

[70] P. Zhang, Y. Sun, H. Jiang, and W. Yao, *Multiscale methods for inverse modeling in 1-d MOS capacitor*, J. Comput. Math., 21 (2003), pp. 85–100.